J. Fluid Mech. (2011), *vol.* 681, *pp.* 370–410. © Cambridge University Press 2011
doi:10.1017/jfm.2011.204

Unsteady boundary-layer transition in low-pressure turbines

JOHN D. COULL† AND HOWARD P. HODSON

Whittle Laboratory, University of Cambridge, Cambridge CB3 0DY, UK

(Received 1 June 2010; revised 28 March 2011; accepted 5 May 2011;
first published online 1 July 2011)

This paper examines the transition process in a boundary layer similar to that present over the suction surfaces of aero-engine low-pressure (LP) turbine blades. This transition process is of significant practical interest since the behaviour of this boundary layer largely determines the overall efficiency of the LP turbine. Modern 'high-lift' blade designs typically feature a closed laminar separation bubble on the aft portion of the suction surface. The size of this bubble and hence the inefficiency it generates is controlled by the transition between laminar and turbulent flow in the boundary layer and separated shear layer. The transition process is complicated by the inherent unsteadiness of the multi-stage machine: the wakes shed by one blade row convect through the downstream blade passages, periodically disturbing the boundary layers. As a consequence, the transition to turbulence is multi-modal by nature, being promoted by periodic and turbulent fluctuations in the free stream and the inherent instabilities of the boundary layer. Despite many studies examining the flow behaviour, the detailed physics of the unsteady transition phenomena are not yet fully understood. The boundary-layer transition process has been studied experimentally on a flat plate. The opposing test-section wall was curved to impose a streamwise pressure distribution typical of modern high-lift LP turbines over the flat plate. The presence of an upstream blade row has been simulated by a set of moving bars, which shed wakes across the test section inlet. Further upstream, a grid has been installed to elevate the free-stream turbulence to a level believed to be representative of multi-stage LP turbines. Extensive particle imaging velocimetry (PIV) measurements have been performed on the flat-plate boundary layer to examine the flow behaviour. In the absence of the incoming bar wakes, the grid-generated free-stream turbulence induces relatively weak Klebanoff streaks in the boundary layer which are evident as streamwise streaks of low-velocity fluid. Transition is promoted by the streaks and by the inherent inflectional (Kelvin–Helmholtz (KH)) instability of the separation bubble. In unsteady flow, the incoming bar wakes generate stronger Klebanoff streaks as they pass over the leading edge, which convect downstream at a fraction of the free-stream velocity and spread in the streamwise direction. The region of amplified streaks convects in a similar manner to a classical turbulent spot: the leading and trailing edges travel at around 88% and 50% of the free-stream velocity, respectively. The strongest disturbances travel at around 70% of the free-stream velocity. The wakes induce a second type of disturbance as they pass over the separation bubble, in the form of short-span KH structures. Both the streaks and the KH structures contribute to the early wake-induced transition. The KH structures are similar to those observed in the simulation of separated flow transition with high free-stream turbulence by McAuliffe & Yaras (*ASME J. Turbomach.*, vol. 132, no. 1, 2010, 011004),

† Email address for correspondence: jdc38@cam.ac.uk

https://doi.org/10.1017/jfm.2011.204 Published online by Cambridge University Press

who observed that these structures originated from localised instabilities of the shear layer induced by Klebanoff streaks. In the current measurements, KH structures are frequently observed directly under the path of the wake. The wake-amplified Klebanoff streaks cannot affect the generation of these structures since they do not arrive at the bubble until later in the wake cycle. Rather, the KH structures arise from an interaction between the flow disturbances in the wake and localised instabilities in the shear layer, which are caused by the weak Klebanoff streaks induced by the grid turbulence. The breakdown of the KH structures to small-scale turbulence occurs a short time after the wake has passed over the bubble, and is largely driven by the arrival of the wake-amplified Klebanoff streaks from the leading edge. During this process, the re-attachment location moves rapidly upstream. The minimum length of the bubble occurs when the strongest wake-amplified Klebanoff streaks arrive from the leading edge; these structures travel at around 70% of the free-stream velocity. The bubble remains shorter than its steady-flow length until the trailing edge of the wake-amplified Klebanoff streaks, travelling at 50% of the free-stream velocity, convect past. After this time, the reattachment location moves aft on the surface as a consequence of a calmed flow region which follows behind the wake-induced turbulence.

Key words: boundary layers, boundary layer separation, transition to turbulence

1. Introduction

The performance of the low-pressure turbine strongly depends on the behaviour of the nominally two-dimensional boundary layer over the blade suction surfaces. In modern 'high-lift' blade designs, this boundary layer is subjected to a region of favourable pressure gradient (FPG) followed by a region of adverse pressure gradient (APG), in which a laminar separation bubble forms. The separation bubble may inflict a considerable aerodynamic penalty, particularly at low Reynolds numbers when it tends to be large (Coull, Thomas & Hodson 2010). The size of the bubble is controlled by the transition between laminar and turbulent flow in the boundary layer, and the details of this process are therefore of great practical interest.

The transition process is complicated by the unsteadiness of the flow in the multi-stage LP turbine. The influence of the adjacent upstream blade row is illustrated in figure 1, which shows a stator wake convecting through a downstream rotor passage. The velocity triangles for both the free-stream flow and the wake fluid are shown in figure 2. In the absolute (stator) frame of reference, the wakes have a lower velocity than the free-stream flow; in the relative (rotor) frame of reference, this velocity deficit may be considered as a 'negative jet' superimposed onto the free-stream flow. As the stator wakes convect through the downstream rotor passage, they impinge onto the suction surface boundary layer, causing the free-stream velocity to first increase and then decrease. In addition to this large-scale velocity perturbation, the negative jet transports turbulent wake fluid to the edge of the boundary layer. These disturbances periodically induce early transition in the boundary layer, a process typically referred to as wake-induced transition. In addition to the wakes arriving from the blade row immediately upstream, the background turbulence is also high as a consequence of wakes shed by components further upstream in the machine. The transition process in the suction surface boundary layer is therefore multi-modal and periodic in time.

https://doi.org/10.1017/jfm.2011.204 Published online by Cambridge University Press

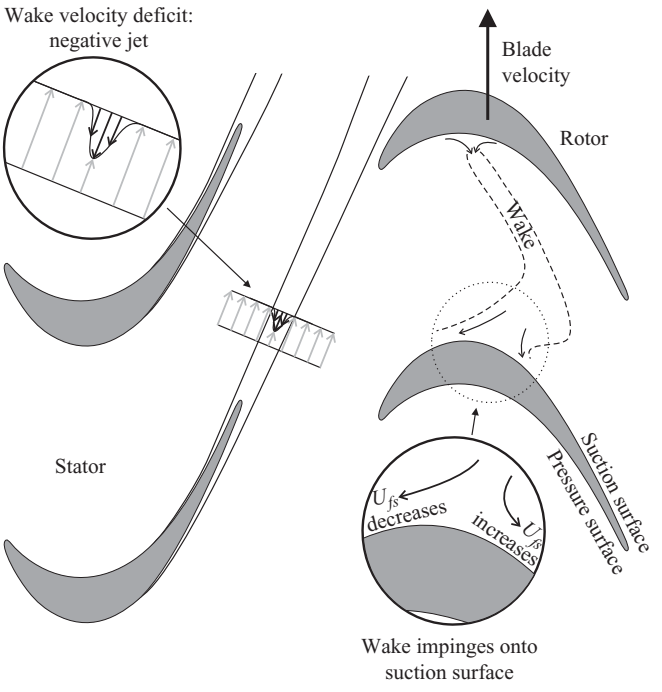


FIGURE 1. Simplified schematic of stator wakes convecting through a downstream rotor passage, based on the data of Stieger & Hodson (2005).

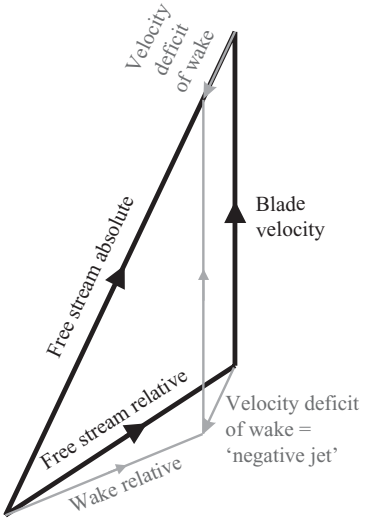


FIGURE 2. Velocity triangles for figure 1: freestream (black) and wake flow (grey).

1.1. *Routes to transition*

Prior to the subsequent discussions of wake-induced transition, it is necessary to consider some more general aspects of transition. To this end, figure 3 shows a diagram of the transition processes identified in this study. This diagram will be referred to throughout this paper as the experimental evidence is presented, and is intended to show the specific transition processes in a more general context.

https://doi.org/10.1017/jfm.2011.204 Published online by Cambridge University Press

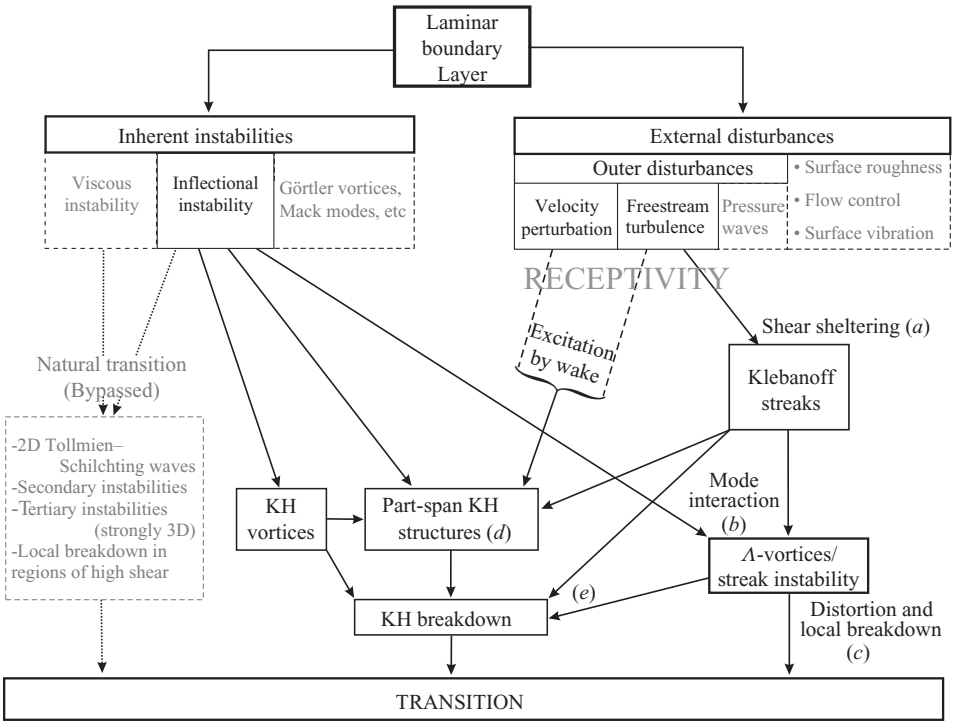


FIGURE 3. Routes to transition identified in the current experiments.

A laminar boundary layer may develop fluctuations which act to promote transition. These fluctuations may arise from the inherent instabilities of the laminar boundary layer, or can be induced by external sources.

1.1.1. *Inherent instabilities*

Above a critical Reynolds number, a laminar boundary layer will become inherently unstable, such that small fluctuations of selective frequencies are amplified. This process is well captured by linear stability analysis via the Orr–Sommerfeld equation (e.g. Schlichting 1979). The instability may be viscous by nature, or, if the free-stream flow is decelerating, the boundary-layer profile will be inflectional and will exhibit inviscid instability.

For attached flow with low free-stream turbulence levels, the transition process proceeds via the 'natural' transition route, indicated in grey on the left-hand side of figure 3. Selective frequencies of background disturbances are gradually amplified, generating two-dimensional Tollmien–Schlichting (TS) waves which develop three-dimensional secondary and tertiary instabilities. Local flow breakdown occurs in regions of high shear, forming turbulent spots which grow and coalesce into a fully turbulent boundary layer. In many turbomachinery flows, this natural transition route is bypassed by other mechanisms; nevertheless, the TS instability can play an important role in the ultimate breakdown to transition, particularly in compressors (e.g. Hughes & Walker 2001).

In strongly decelerating flow, a laminar boundary layer will separate from the surface. In a similar manner to inflectional attached boundary layers, the separated shear layer exhibits inviscid instability due to the strongly inflectional profile (Diwan & Ramesh 2009). This instability is referred to as the Kelvin–Helmholtz (KH) instability

https://doi.org/10.1017/jfm.2011.204 Published online by Cambridge University Press

because of the similarities with a free shear layer, and tends to drive the roll-up of the separated shear layer into coherent vortices. In general, these vortices may be coherent in the spanwise direction (i.e. two-dimensional) or at an oblique angle to the flow direction. In low free-stream turbulence conditions, transition is driven by either the KH instability of the separated shear layer, instability waves convecting from the upstream boundary layer or by a combination of the two.

While the inviscid instability of the boundary layer is of primary importance in this study, in general other inherent instability modes may be exhibited (indicated in grey in figure 3). For example, Marxen *et al.* (2009) found evidence of Görtler vortices induced by the concave streamlines close to laminar separation. However, no evidence of such vortices was observed in the current measurements.

1.1.2. *External disturbances*

A laminar boundary layer may be subjected to external sources of disturbance, which originate either at the surface or in the free-stream flow. This paper is concerned only with the latter case. Provided that the boundary layer is receptive to the external disturbances, fluctuations will be induced in the boundary layer, which will tend to bypass the slow amplification of small disturbances that occurs in the early stages of natural transition.

Turbulent fluctuations in the free-stream generate streaky structures in the boundary layer, which are typically referred to as 'Klebanoff modes'. This terminology is misleading as these are continuous rather than modal instabilities (in the eigenvalue sense). The term 'Klebanoff streaks' will therefore be used in preference. These structures are generated in the thin boundary layer close to the leading edge in a receptivity process often referred to as 'shear sheltering'; whereby the mean shear of the boundary layer tends to damp high-frequency disturbances, while the low-frequency disturbances penetrate and disturb the boundary layer (Jacobs & Durbin 2001). This process has been labelled (*a*) in figure 3. Jacobs & Durbin (1998) analysed the Orr–Sommerfeld equations and showed that the penetration depth of a free-stream disturbance into the boundary layer increases with reducing disturbance frequency and Reynolds number (based on the boundary-layer thickness). The boundary layer near the leading edge of an aerofoil is therefore a key receptivity site for Klebanoff streaks because the Reynolds number is low and the wavelengths of the free-stream disturbances are large compared to the boundary-layer thickness.

Marxen *et al.* (2009) examined the growth of Klebanoff streaks in a flat-plate boundary layer subjected to a favourable pressure gradient (FPG) followed by a region of adverse pressure gradient (APG), which featured a laminar separation bubble. In the stable FPG region, spatial transient growth was observed, driven by the uplift of the streaks from the surface. At the start of the APG region, Marxen *et al.* (2009) found that the growth of the Klebanoff streaks was also driven by a modal Görtler instability, induced by the concave streamlines close to separation.

Durbin, Zaki & Liu (2009) used direct numerical simulations (DNS) to examine the interaction between Klebanoff streaks and the inherent instabilities of a laminar boundary layer. Initial simulations with either streaks or Tollmien–Schlichting (TS) waves in isolation did not show transition to turbulence. In the presence of both disturbances, the Klebanoff streaks interacted with the TS waves to generate Λ-vortices (process *b* in figure 3). These structures lifted away from the surface and experienced local breakdown to form turbulent spots (process *c* in figure 3).

The simulations of McAuliffe & Yaras (2010) examined the influence of free-stream turbulence on separated flow transition. At low free-stream turbulence (0.15%), the

https://doi.org/10.1017/jfm.2011.204 Published online by Cambridge University Press

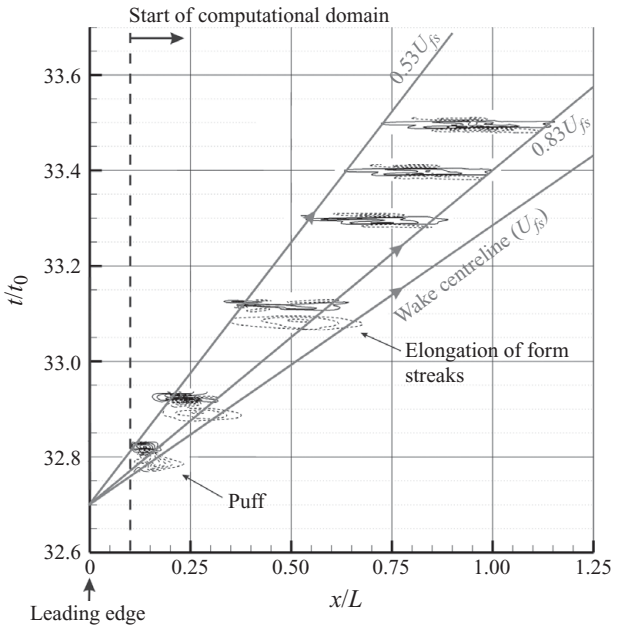


FIGURE 4. The evolution of a wake-induced streak, visualised by contours of U_x' (solid lines: negative; dashed lines: positive), derived from the DNS simulation of Wu *et al.* (1999).

KH instability dominated the transition process and full-span vortices were shed from the separation bubble. Transition proceeded more rapidly in the high turbulence (1.45%) case, where Klebanoff streaks arriving at separation distorted the separated shear layer, which became highly three-dimensional. In this case, full-span KH vortices were not observed, but short-span KH vortex structures occasionally formed where the distorted shear layer was locally unstable. The findings of McAuliffe & Yaras (2010) will be compared to the current results later in this paper.

1.2. *Previous investigations of wake-induced transition*

Key investigations of wake-induced transition will now be considered. The relevance of some of these studies to real-engine behaviour is questionable because of differences between real-engine flow conditions and the experimental or numerical set-ups; nonetheless they are useful for understanding the fundamental boundary-layer behaviour.

1.2.1. *Wake-induced streaks*

Wu *et al.* (1999) performed DNS of wake-induced transition in an attached flat-plate boundary layer with zero pressure gradient. The computational domain excluded the flat-plate leading edge, and the turbulence intensity in the free-stream flow between the wakes was zero. The results showed that the turbulent fluid in the wake induces transition in a somewhat similar manner to bypass transition in attached flow (e.g. Jacobs & Durbin 2001). Figure 4 shows the evolution of a wake-induced structure on a space–time plot, which has been derived from figure 17 in Wu *et al.* The 'puff' originating at the inlet of the computational domain ($x/L = 0.1$) stretches into a streaky structure as it convects downstream. A line has been drawn on this plot to indicate the path of the wake centreline over the flat-plate surface at the free-stream velocity U_{fs} (interpolated from figure 7 in Wu *et al.*). The streak convects more slowly

https://doi.org/10.1017/jfm.2011.204 Published online by Cambridge University Press

than the free-stream flow: two further lines show the approximate paths of the streak leading and trailing edges, which, in this case, have convection speeds of $0.83\,U_{fs}$ and $0.53\,U_{fs}$, respectively. These convection rates are similar to the leading and trailing edge celerities of a turbulent spot in zero pressure gradient, which are $0.88\,U_{fs}$ and $0.5\,U_{fs}$, respectively (Schubauer & Klebnaoff 1955).

The simulation of Wu *et al.* was performed on a zero pressure gradient flat plate with low free-stream turbulence, which is not representative of engine conditions. The exclusion of the leading edge region ($x/L < 0.1$) from the computational domain also raises concern since this region is a crucial receptivity site for Klebanoff streaks. Despite these apparent deficiencies, a similar process is evident in the current measurements, and comparable propagation rates to those in figure 4 were observed.

1.2.2. *Excitation of the KH instability*

Stieger & Hodson (2004) examined wake-induced transition experimentally using a linear cascade of T106 high-lift turbine blades at low free-stream turbulence. This blade features a closed separation bubble on the aft portion of the suction surface. Phase-averaged laser Doppler anemometry measurements showed that KH roll-up vortices formed as the wake passed over the separated shear layer. These vortices distorted as they convected downstream and broke down to small-scale turbulence. The complementary DNS studies of Wissink, Rodi & Hodson (2006) confirmed that a full-span roll-up of the shear layer is driven by the large-scale velocity perturbation of the wake (figure 1) as it convects over the bubble.

Opoka & Hodson (2008) examined the effect of free-stream turbulence, performing unsteady pressure measurements on the T106 suction surface. At low free-stream turbulence (0.5%), pressure perturbations caused by the wake-induced roll-up of the shear layer were observed. At a high free-stream turbulence level (4%), these perturbations were diminished or suppressed entirely, implying that the free-stream turbulence modifies the bubble behaviour. However, the nature of the change in flow behaviour was not clear. Direct simulations of unsteady wake-induced transition have yet to be performed with realistic levels of free-stream turbulence between the wakes. However, it is useful to consider the simulations of McAuliffe & Yaras (2010), discussed in the previous section, who found that the Klebanoff streaks distorted the separated shear layer, preventing the formation of full-span roll-up vortices.

The current work aims to shed further light on the wake-induced transition process with separated flow and high free-stream turbulence, and examine the role of Klebanoff streaks and the KH instability of the bubble. The following section details the experimental methods and processing techniques employed (see § 2). The time- and phase-averaged data are then discussed (see § 3) before the instantaneous measurements are examined (see § 4) and the conclusions are summarised (see § 5).

2. Experimental methods and data processing

2.1. *Decomposition of flow parameters*

In steady flow, a flow parameter X may be separated into a time-mean ($\bar{X}$) and a fluctuating component ($X'(t)$), such that

$$X(t) = \bar{X} + X'(t). \tag{2.1}$$

In a periodic flow, it is more appropriate to perform a decomposition relative to the phase-averaged quantity $\langle X(t)\rangle$

$$X(t) = \langle X(t)\rangle + X'(t) = \overline{X} + \tilde{X}(t) + X'(t), \tag{2.2}$$

https://doi.org/10.1017/jfm.2011.204 Published online by Cambridge University Press

Suction surface length S_0 (from stagnation point)	(mm)	505
Span	(mm)	458
Plate thickness	(mm)	12.8
Semi-major-axis of elliptical leading edge	(mm)	38
Freestream turbulence intensity $U_{rms}/\bar{U}$		3.0%
Freestream turbulence integral length scale	(mm)	30.1
Bar diameter	(mm)	7.8
Axial distance: bars to leading edge	(mm)	465
Bar pitch	(mm)	720
Reduced frequency $f_r = f_{wake}S_0/U_{TE}$		0.84

TABLE 1. Specification of flat-plate test rig and moving bar mechanism.

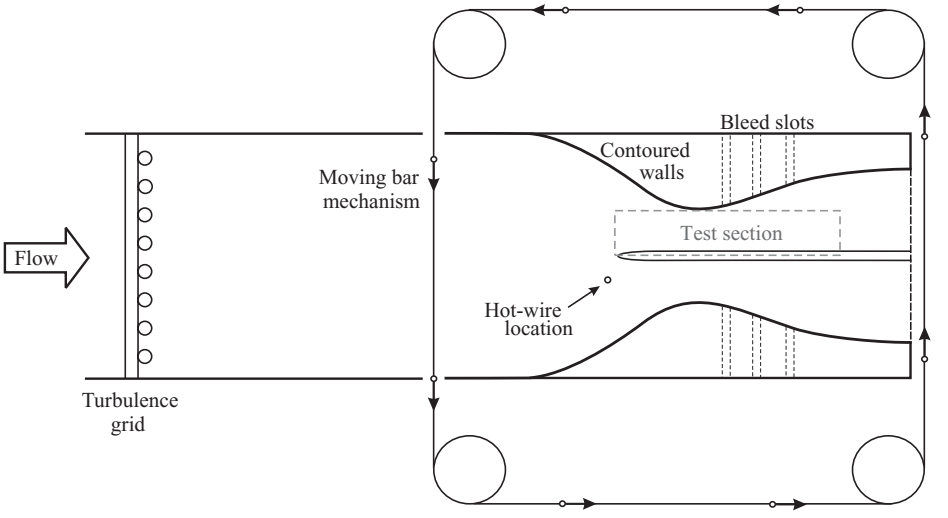


FIGURE 5. Schematic of the flat-plate experiment.

where $\tilde{X}(t)$ is the perturbation quantity and the time-mean $\bar{X}$ is given by the time-mean of the phase-average

$$\overline{X} = \overline{\langle X(t) \rangle}. \tag{2.3}$$

The root-mean-squared (r.m.s.) level of fluctuation is defined for both steady and periodic flows as

$$X_{rms} = \overline{\sqrt{(X')^2}}. \tag{2.4}$$

2.2. *The flat-plate rig*

The suction surface boundary layer of an LP turbine blade has been simulated on the flat plate shown in figure 5, which is designed to simulate the aerodynamic unsteadiness that is inherent in a multi-stage LP turbine. A streamwise pressure distribution was imposed along the surface by installing contoured walls above and below the flat plate. To avoid flow separation on the liners, bleed slots were cut into the surfaces (figure 5) and the test section was pressurised by means of an adjustable exit grid. The main design parameters of the flat plate are summarised in table 1. The aluminium flat-plate is 738 mm long, 458 mm wide and 12.8 mm thick. Measurements

https://doi.org/10.1017/jfm.2011.204 Published online by Cambridge University Press

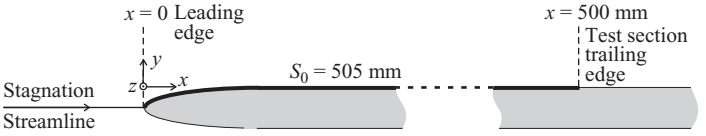


FIGURE 6. Definition of the reference length S_0 and co-ordinate system.

have been performed over the first 500 mm of the upper surface of the plate (the 'test section' in figure 5). The leading edge is elliptical, with a semi-major-axis of 38 mm. Eleven static tappings uniformly distributed around the leading edge ellipse were used in setting the incidence to zero; oil-and-dye flow visualisation indicated that there was no leading edge separation bubble at this condition. Incidence was controlled by independently adjusting the blockage at the exit of the top and bottom sections. Thirty-three static pressure tappings (0.3 mm diameter) and 16 hot-films were distributed along the length of the plate. These were placed at 40% and 60% of the span, respectively. The inlet total pressure and temperature were measured close to the leading edge.

Apart from the elliptical leading edge, the flat-plate rig does not model the surface curvature of a real turbine blade. One must therefore consider how important this effect is. The pressure gradient in the wall-normal direction depends on the ratio of the boundary-layer thickness δ to the surface curvature R (White 1999). This parameter was estimated for the T106 turbine blade using the quasi-two-dimensional flow solver MISES (version 2.0) at a comparable Reynolds number to the current tests. With the exception of the leading edge region, the ratio δ/R was found to be less than 0.03 over the suction surface, indicating that surface curvature will have only a secondary influence on the boundary-layer development.

By convention, turbine Reynolds numbers are based on the mean exit velocity from the blade row. In order to provide an equivalent reference position, a 'nominal trailing edge' has been chosen on the flat-plate surface, at a streamwise distance of 500 mm from the leading edge. The reference velocity U_{TE} is taken as the time-mean free-stream velocity at this location. (Throughout this paper, the free-stream velocity is taken as the streamwise velocity component above the boundary layer.) The reference length S_0 is the surface length between the leading edge stagnation point and the nominal trailing edge, which is illustrated in figure 6. This length is equivalent to the suction surface length of a curved turbine blade. Together with the kinematic viscosity ν, the Reynolds number is therefore defined as

$$Re_{S_0} = \frac{U_{TE} S_0}{\nu}. \tag{2.5}$$

Figure 6 indicates the co-ordinate system used throughout this paper, where x, y and z indicate the streamwise, wall-normal and spanwise directions, respectively. The positive z-direction points out of the page in figure 6. Downstream of the elliptical leading edge, $y = 0$ corresponds to the upper surface of the flat plate.

Data were collected at a Reynolds number $Re_{S_0} = 84,000$, which is low for large civilian aircraft engines and is more representative of the LP turbines in a small business jet or unmanned aerial vehicle. This test Reynolds number has been selected for several reasons: the separation bubble will tend to be large and so the performance strongly depends on the transition onset location; the thicker boundary layer permits a better spatial resolution of the measurements; and the test Reynolds number is low

https://doi.org/10.1017/jfm.2011.204 Published online by Cambridge University Press

enough to enable complementary DNS calculations to be performed in the future. At Reynolds numbers above that tested, transition proceeds more rapidly, and the balance between the different sources of instability may change. However, one would expect to observe the same underlying mechanisms driving the transition process, provided that the boundary layer still features a laminar separation bubble. For modern high-lift LP turbines, this is likely to be the case for $Re_{S_0} < 290\,000$ (Coull, Thomas & Hodson 2010).

2.3. *Unsteady inflow conditions*

The turbulence grid and moving bar mechanism in figure 5 have been designed to match the turbulence and wake properties measured by Halstead (1996) in the final stage of a three-stage research turbine.

The turbulence grid was installed upstream of the flat plate to elevate the free-stream turbulence level in the test section. The grid consisted of sets of horizontal and vertical round bars of 20 mm diameter with gaps of 50 mm between bars, and was installed at a distance of 1.750 m upstream of the flat-plate leading edge. To confirm the characteristics of the grid-generated turbulence, a static single-element hot-wire was installed close to the leading edge of the flat plate, as indicated in figure 5. The axis of the hot-wire sensing element was in the spanwise (z) direction. The output was logged for 60 s using a sampling rate of 20 kHz. The results demonstrated that the r.m.s. level of the velocity fluctuations was approximately 3.0% of the time-mean value. The integral length scale was calculated to be 30.1 mm by integrating the autocorrelation of the fluctuating component of velocity up to the first zero crossing.

The design parameters of the moving bar mechanism are included in table 1. A hot-wire measurement was performed to confirm the properties of the wakes, and 128 phase-locked datasets were obtained. The r.m.s. of the measured velocity traces ($\langle U_{rms} \rangle / \langle U \rangle$) is presented in figure 7(a) and reaches a peak level of 6% in the wake centre, dropping to the background level of 3% between wakes. The ensemble-averaged velocity has been presented in figure 7(b) alongside a raw velocity trace. The phase-averaged velocity reaches a minimum of around $0.94\overline{U}$ close to the wake centre. The r.m.s. shown in figure 7(a) contains no information about the scales of the unsteadiness. Traditional Fourier analysis is limited for such periodic signals, since the spectrum of the wakes cannot be easily extracted from the background turbulence. To overcome this problem, wavelet analysis has been performed using the technique described in detail by Lewalle, Ashpis & Sohn (1997). The continuous wavelet transform is first computed using the Morlet wavelet. The coefficients are then squared and smoothed using a Gaussian filter with a width equal to the wavelet scale. The resultant local energy spectrum density (LESD) is analogous to the power spectral density (PSD) in Fourier analysis, but it is localised in time. The phase-averaged LESD is presented in figure 8 for a range of frequencies, effectively showing the time-dependent PSD for different frequencies. This plot demonstrates that the wakes contain fluctuations over a large range of frequencies, right up to the noise floor of the data ($\sim 200 f_{wake}$).

The frequency of the incoming wakes is non-dimensionalised using the approximate transit time of the test section, S_0/U_{TE}, to give the reduced frequency

$$f_r = \frac{f_{wake}\, S_0}{U_{TE}} = \frac{S_0}{U_{TE}\, t_0}, \tag{2.6}$$

https://doi.org/10.1017/jfm.2011.204 Published online by Cambridge University Press

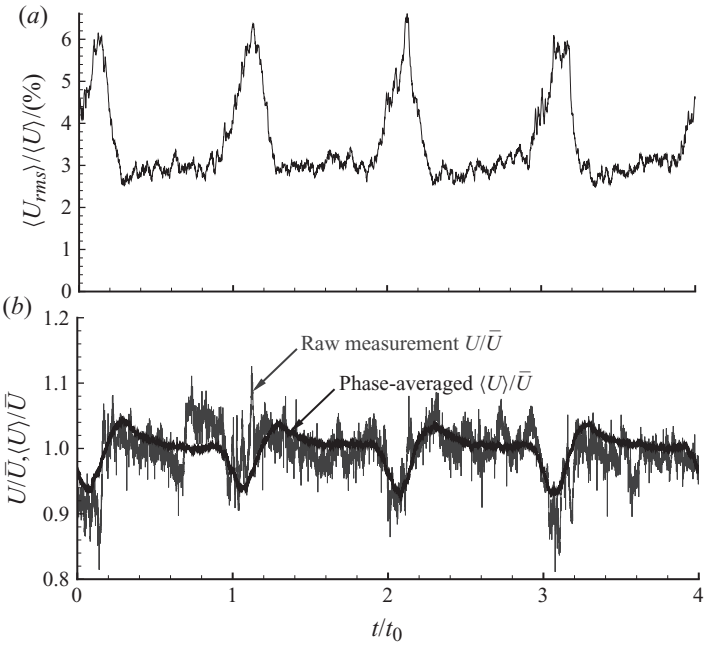


FIGURE 7. Wake characteristics from single-element hot-wire: (*a*) r.m.s. fluctuations; (*b*) raw and phase-averaged velocity.

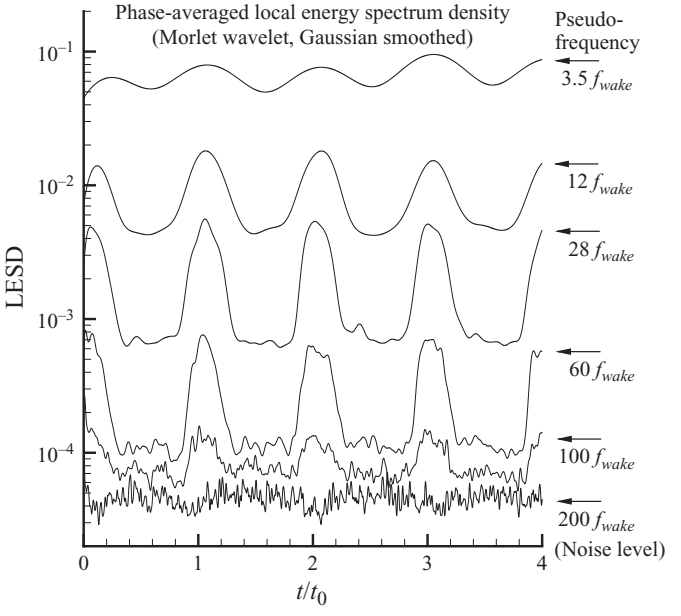


FIGURE 8. Phase-averaged frequency components of the inlet hot-wire data; local energy spectrum density via wavelet analysis (Lewalle *et al.* 1997).

where f_{wake} and t_0 are the frequency and period of the incoming wakes. The current measurements have been performed without incoming wakes ('steady flow') and at a reduced frequency of $f_r = 0.84$, which is representative of aero-engine LP turbines.

https://doi.org/10.1017/jfm.2011.204 Published online by Cambridge University Press

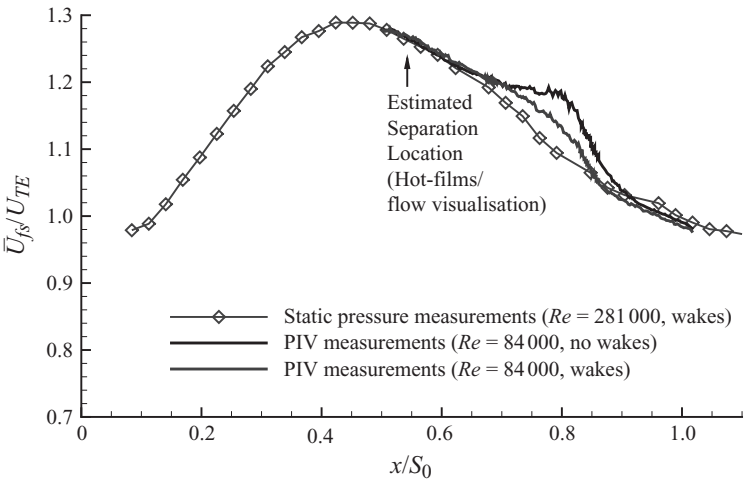


FIGURE 9. Time-averaged free-stream velocity distribution over the flat plate.

2.4. *Free-stream velocity distribution*

Time-averaged measurements of the static pressure along the blade surface were performed using a Scanivalve DSA 3017 16-channel pressure scanner with a range of 2500 Pa and a 0.125 Pa resolution. The derived free-stream velocity distribution, is shown in figure 9 for a Reynolds number of $Re_{S_0} = 281\,000$. At the test Reynolds number of 84 000, the dynamic pressures in the test section were very low and the static pressure measurements suffered from a high level of noise. Instead, the time-mean free-stream velocity obtained from PIV measurements along the mid-span is included in figure 9 for both steady and unsteady flow. In general, the free-stream (inviscid) flow in the passage tends to have a very slight gradient normal to the flat plate surface (i.e. $\mathrm{d}U_x/\mathrm{d}y$ is small but not zero). To find the free-stream velocity, a linear regression analysis was applied to the measurement points above the boundary layer. The location where the boundary-layer velocity profile first reaches this line is taken as δ_{100}, and the free-stream velocity U_{fs} is measured at this point. Figure 9 shows that the flow accelerates over the front portion of the surface up to the peak velocity location $x/S_0 = 0.42$. As the flow decelerates downstream of this point, the boundary layer separates at around $x/S_0 \approx 0.54$ (estimated below from hot-film measurements and oil-and-dye flow visualisation). Transition occurs in the separated shear layer and the flow re-attaches to form a closed bubble. This velocity distribution was previously designated as Design C in the study of Coull, Thomas and Hodson (2010). This design has a higher 'loading' than the T106 blade used in previous studies (e.g. Stieger & Hodson 2004; Opoka & Hodson 2008) and is more representative of the latest generation of high-lift LP turbine designs.

2.5. *Particle imaging velocimetry*

A LaVision system has been used to perform PIV measurements. Laser light was provided by two pulsed Nd-YAG lasers and the typical thickness of the light sheet was less than 1 mm. Images were recorded with double-frame 12-bit digital cameras with a 1280×1024 CCD array, and post-processed using the DaVis software supplied by LaVision. The maximum data rate of the current system was limited by the data transfer rate of the cameras to around 7 Hz, which is too low to obtain sequential

https://doi.org/10.1017/jfm.2011.204 Published online by Cambridge University Press

images of the flow field; rather, measurements were performed at fixed intervals in the wake cycle. Two different PIV configurations have been used.

Two-dimensional PIV measurements were obtained in a plane normal to the flat-plate surface along the mid-span of the flat plate at three separate streamwise locations, centred at approximately $x/S_0 = 0.60, 0.75$ and 0.95. The measurement window size was approximately 50 mm × 90 mm. Approximately 250 instantaneous measurements were collected at eight equally spaced time-steps through the wake-passing period, and for steady flow (with elevated turbulence but without the incoming wakes). The processing used a final interrogation window size of 32×32 pixels with a 50% overlap, giving a spatial resolution of approximately 1 mm.

To examine the spanwise nature of the flow, stereoscopic PIV measurements were performed in planes parallel to the flat-plate surface, with a measurement window size of approximately 50 mm × 60 mm. Two different streamwise positions were examined at five different heights through the boundary layer. Measurements from two of these locations will be presented in this paper. At least 130 instantaneous measurements were obtained for steady flow and for a total of 11 time-steps through the wake cycle. These time-steps included the eight equally spaced time-steps used in the mid-span measurements and three additional time-steps. Processing was performed using a final interrogation window size of 16×16 pixels with a 50% overlap, giving a spatial resolution of approximately 0.4 mm. The finer resolution in the wall-parallel data compared to the wall-normal data was possible due to the absence of any surface reflections in the wall-parallel set-up.

2.6. *Surface hot-film anemometry*

Surface-mounted hot films were used to measure wall shear stress in a semi-quantitative manner, using the quasi-wall shear stress (Hodson 1983)

$$\tau_w = \left(\frac{E^2 - E_0^2}{E_0^2} \right)^3, \tag{2.7}$$

where E is the hot-film bridge output voltage and E_0 is its value under zero-flow conditions. This method of data reduction allows the relative magnitude of the shear stress to be compared between sensors without the need for elaborate calibration.

The hot-film sensors used in the current study were Tao Systems Senflex 9101 sensors, which were operated in constant temperature mode using Dantec 56C01/56C16 anemometers. The output signals were passed through Dantec 55N22 signal-conditioning units. The DC and AC components of these signals were logged separately. The AC component was low-pass filtered at 10 kHz and acquired at a frequency of 20 kHz. A total of 256 ensembles of raw data were recorded for several wake passing periods.

Due to the low levels of shear stress in the test section, the AC components of the hot-film signals suffered from poor signal-to-noise ratio. Three examples of raw signal outputs are presented in figure 10(*a–c*), which, respectively, show measurements obtained in regions of attached laminar flow, separated flow and intermittent turbulent reattachment. Note the different ordinate scale for figure 10(*c*). High-frequency white noise is evident in the data, which was removed using a wavelet-based method which minimises the loss of data in the de-noising process. The signal was first decomposed into different frequency components using the discrete stationary wavelet transform and the Daubechies 5 wavelet. The background noise was then removed using manually-set thresholds for each frequency component and the signal was reconstructed. An overview of similar de-noising processes may be found in Cai &

https://doi.org/10.1017/jfm.2011.204 Published online by Cambridge University Press

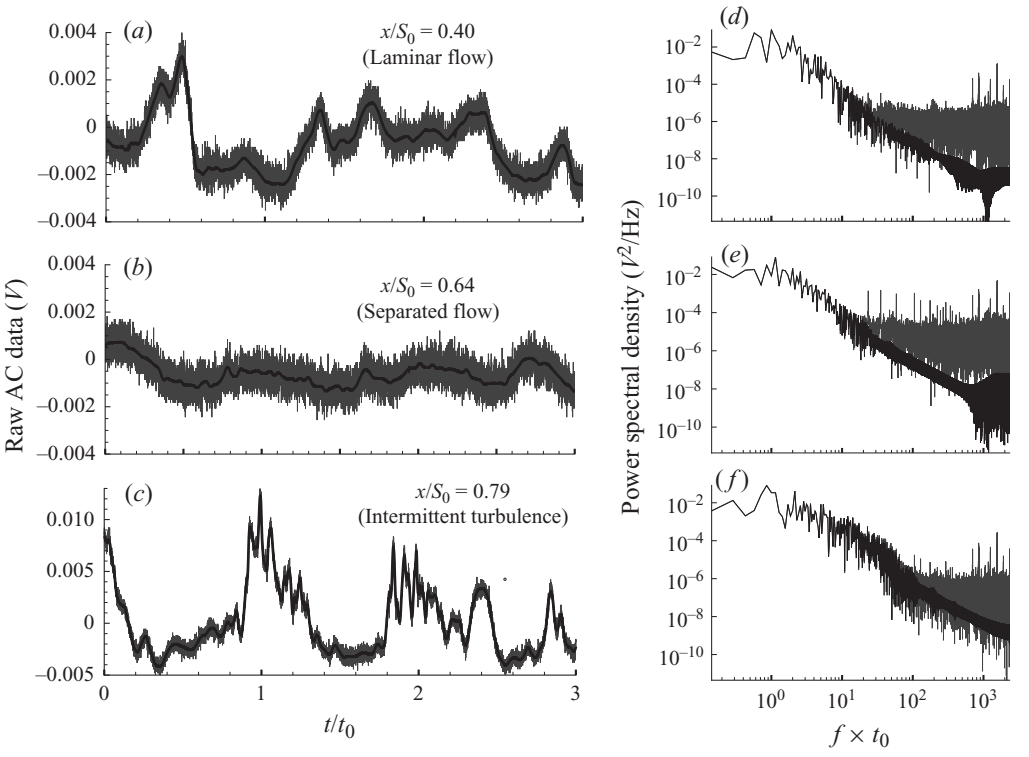


FIGURE 10. (*a–c*) Raw AC hot-film traces (grey) and de-noised signals (black); (*d*)–(*f*) corresponding spectra.

Harrington (1998). The de-noised signals are shown alongside the raw traces in figure 10(*a–c*) and the power spectra are compared in figure 10(*d–f*).

3. Time-mean and phase-averaged results

This section presents both the time-mean of the steady flow measurements (with elevated free-stream turbulence but without incoming wakes) and the phase-average of the unsteady flow measurements. The results reveal important information about the boundary-layer behaviour and the effects of the incoming wakes, setting the scene for the discussion of the instantaneous measurements in the subsequent section.

3.1. *Time-mean steady flow*

From the PIV measurements, velocity profiles along the flat-plate mid-span are presented in figure 11(*a*) for steady flow. Note that the vertical axis has been stretched to enable the boundary layer to be clearly shown. The lines joining the data points have been extended to indicate zero velocity at the wall. The approximate outline of the reversed flow region and the line of inflection have been indicated, along with the edge of the boundary layer δ_{95}. Due to the limited spatial resolution of the PIV data, the inner regions of the velocity profiles are not well defined. Estimated errors in $\overline{U_x}$ are shown in figure 11(*b*) for a sample profile. These are a combination of typical bias errors for the LaVision post-processing algorithm (Stanislas *et al.* 2005) and estimated convergence errors (due to the finite number of datasets averaged). The vectors closest to the wall suffer from the greatest uncertainty due to surface reflections and relatively

https://doi.org/10.1017/jfm.2011.204 Published online by Cambridge University Press

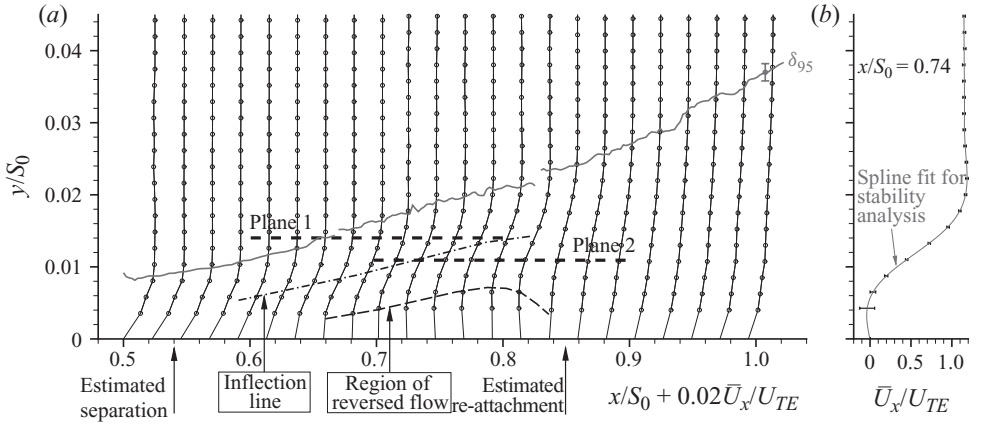


FIGURE 11. (*a*) Time-mean velocity profiles along the flat-plate mid-span for steady flow, the horizontal lines indicate the location of the wall-parallel measurement planes; (*b*) sample velocity profile with estimated errors and spline fit used for stability analysis.

poor seeding in this region. These uncertainties and the poor spatial resolution make it difficult to accurately determine the separation location from the velocity profiles. However, based on hot-film results and oil-and-dye flow visualisation, it is estimated that the flow separates from the surface at around $x/S_0 = 0.54$. The separation bubble grows to a maximum height at around $x/S_0 = 0.79$ before re-attaching at around $x/S_0 = 0.85$.

Dashed lines have been added to figure 11(*a*) to indicate the position of two of the wall-parallel PIV measurement planes. Measurement plane 1 is centred at $x/S_0 = 0.70$, covering the 'laminar' portion of the bubble, at a height of $0.014\,S_0$ from the surface. Since the flow is non-parallel, the location of this plane relative to the thickness of the boundary layer varies with streamwise distance. It sits above the boundary layer for $x/S_0 < 0.65$ and in the outer region of the boundary layer for $x/S_0 > 0.65$, where one might expect to observe local breakdown to turbulence in bypass transition (e.g. Wu *et al.* 1999). Measurement plane 2 is centred at $x/S_0 = 0.80$ and covers the re-attachment region of the bubble near the mid-height of the boundary layer, where one might expect to observe KH vortices in the flow. The orientation and extent of measurement planes 1 and 2 can be observed in, for example, figure 12(*a*) and figure 24, respectively.

Steady flow data from the wall-parallel measurement plane 1 are shown in figure 12(*a*), where a contour plot of the root-mean-square (r.m.s.) of the fluctuation in streamwise velocity ($\langle U_{x\,rms}\rangle/\langle U_x\rangle$) is presented. Around 250 individual measurements have been used to produce this plot. The fluctuations increase with the streamwise distance, an effect which is largely due to the non-parallel nature of the flow. As shown in figure 11(*a*), at downstream locations, measurement plane 1 sits lower in the boundary layer, and therefore captures higher levels of fluctuations. Interestingly, a slight quasi-periodic spanwise variation is visible as 'ripples' in the contour lines. The inset plot in figure 12(*b*) presents the variation in r.m.s. across the span at the streamwise location $x/S_0 = 0.70$. From inspection, the spanwise wavelength is between 0.02 and $0.03S_0$. An estimated error bar has also been indicated on this plot, which is dominated by the convergence error due to the limited number of data samples. Although the uncertainties are large, the observed variations are still significant. The spanwise wavelength has been quantified by calculating the autocorrelation of the

https://doi.org/10.1017/jfm.2011.204 Published online by Cambridge University Press

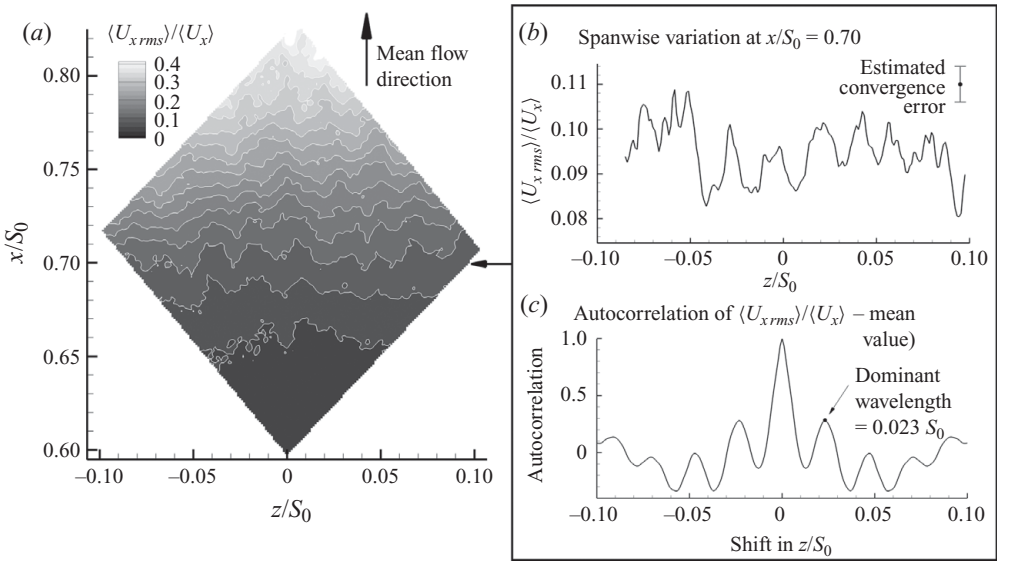


FIGURE 12. r.m.s. of velocity fluctuations ($\langle U_{x\,rms}\rangle/\langle U_x\rangle$) across the span for steady flow, $y/S_0 = 0.014$ (plane 1 in figure 11*a*).

fluctuations, shown in figure 12(*c*). The first peak on this plot indicates a spanwise wavelength of $0.023\,S_0$, which is around 1.5 times the boundary layer thickness δ_{95} at this streamwise location ($0.016\,S_0$, figure 11*a*).

Several authors have observed spanwise variations in separation bubbles through flow visualisation experiments (e.g. Ginoux 1965; Rosko & Thomke 1966) and hot-wire measurements (e.g. Watmuff 1999). In many cases, the wavelength of the spanwise variation is around $2 \rightarrow 4\delta$ at separation, which can be accounted for by a Taylor–Görtler-type instability arising from the concave streamline curvature in the region of re-attachment (Inger 1975) or separation (Marxen *et al.* 2009). The wavelength of the variation observed in the current study is similar, being around 2.5 times the boundary-layer thickness at separation ($\delta_{95} \approx 0.01 S_0$, figure 11). As the boundary layer thickens downstream of separation, this ratio becomes closer to the typical spanwise spacing between Klebanoff streaks in a developed boundary layer (around $1.2\,\delta$, Matsubara & Alfredsson 2001). That the spanwise variation is evident in the time-mean data indicates that the spanwise location of the instantaneous Klebanoff streaks is partially deterministic, and may be fixed by the position of the tunnel walls (located at $z/S_0 = \pm 0.454$), or slight roughness effects at the leading edge where the boundary layer is very thin.

3.2. *Phase-averaged unsteady flow*

The influence of the incoming wake disturbance on the flow behaviour will now be discussed with reference to the phase-averaged measurements.

3.2.1. *The unsteady disturbance environment*

As the wake passes over the boundary layer, it perturbs the free-stream velocity. Figure 13(*a*) shows the phase-averaged $\langle U_{fs}\rangle$ at the streamwise location $x/S_0 = 0.65$, which has been derived from the PIV measurements along the flat-plate mid-span (as for figure 9). The free-stream velocity is initially quasi-steady ($t/t_0 = 0$) between wakes. The arrival of the wake is evident at around $t/t_0 \approx 0.125$, where $\langle U_{fs}\rangle$ starts to

https://doi.org/10.1017/jfm.2011.204 Published online by Cambridge University Press

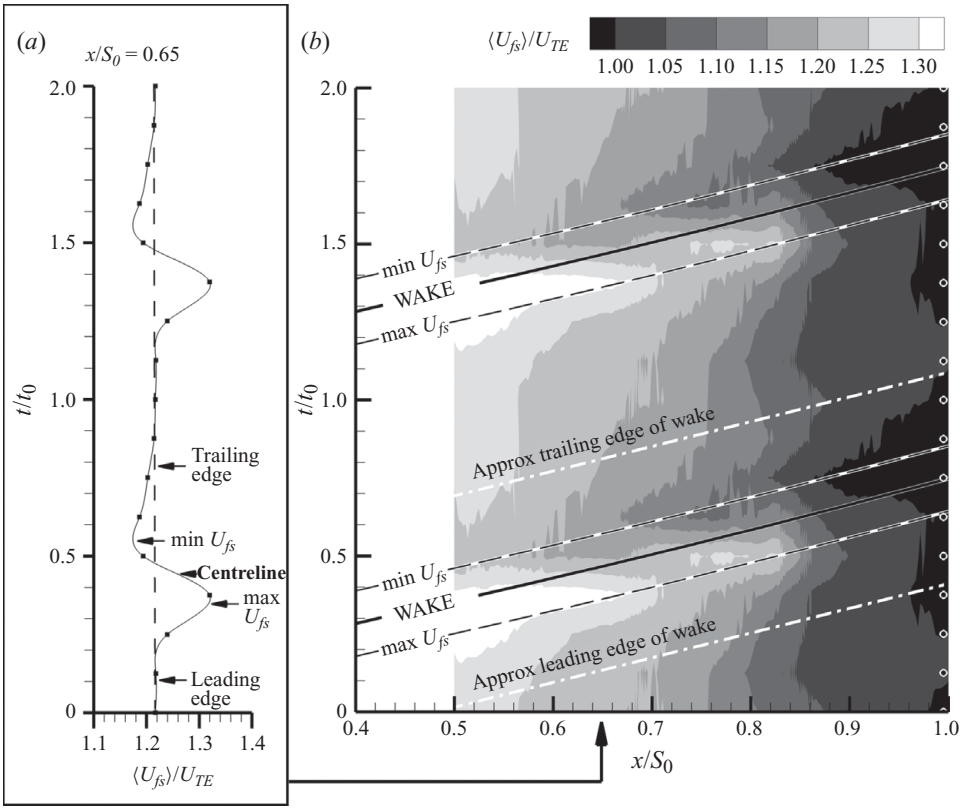


FIGURE 13. Freestream velocity through the wake cycle: (*a*) at a particular streamwise location; (*b*) space-time plot.

increase, reaching a maximum at $t/t_0 \approx 0.35$. The free-stream velocity then decreases, reaching a minimum at $t/t_0 \approx 0.55$ before gradually returning to a quasi-steady value at around $t/t_0 \approx 0.8$. The velocity fluctuations can be explained with reference to the negative jet in figure 1. As the front of the wake passes over the boundary layer, the free-stream velocity increases; as the rear of the wake passes, the free-stream velocity decreases.

In order to show the variation of $\langle U_{fs}\rangle$ over the whole surface, the data are presented as a space–time plot in figure 13(*b*). The data have been repeated for two wake-passing cycles. Dots have been added to the right-hand side of the plot to indicate the temporal resolution of the data. The lines in figure 13(*b*) represent the nominal path of the wakes, which travel at the free-stream velocity. The paths of the lines labelled as 'max U_{fs}' and 'min U_{fs}' have been chosen to approximately coincide with the timings of the maximum and minimum of $\langle U_{fs}\rangle$, respectively, for each streamwise location (as in figure 13*a*). Between these paths, a solid line indicates the path of the wake centreline. Lines have also been drawn to indicate the leading and trailing edge of the wake. The leading edge precedes the wake centreline by around $0.35\,t_0$, with a similar delay between the centreline and the trailing edge.

The r.m.s. of the free-stream velocity $\langle U_{x\,rms}\rangle/\langle U_x\rangle$ has been calculated at the height where the streamwise velocity reaches 95% of the free-stream value (δ_{95}). The data are presented as a space–time diagram in figure 14. The lines representing the path of the wake have been duplicated from figure 13(*b*). To aid the interpretation of the plot,

https://doi.org/10.1017/jfm.2011.204 Published online by Cambridge University Press

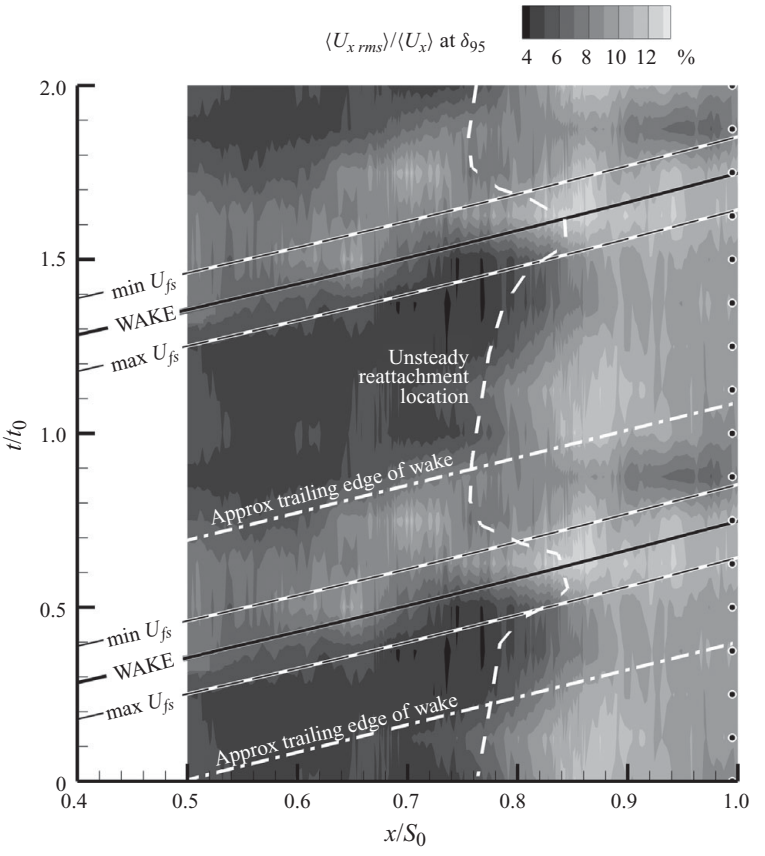


FIGURE 14. Space–time plot of r.m.s. velocity at $y = \delta_{95}$.

a line has been drawn to indicate the approximate location of the unsteady flow re-attachment (this will be derived from figure 15 in the following section). Downstream of this line, the high levels of fluctuations largely originate in the turbulent boundary layer. Upstream of this line, the fluctuations are induced by the wake. Between wakes, the r.m.s. is around 4–5%, and around 3% higher underneath the wake path. The region of high turbulence lags slightly behind the velocity perturbation of the wake, being bounded by the 'max U_{fs}' and the trailing edge of the wake. A similar delay between the velocity perturbation of the wake and the peak r.m.s. fluctuations has been observed previously (e.g. Zhang & Hodson 2007), and this effect appears to be caused by the distortion of the wake as it convects through the passage and impinges onto the boundary layer (Stieger & Hodson 2005).

3.2.2. *The unsteady re-attachment location*

The impinging wakes induce a periodic shortening of the separation bubble compared to the steady flow case. This is most evident in the hot-film data. Contours of phase-averaged quasi-wall shear stress $\langle \tau_w \rangle$ are presented in the space–time plot of figure 15(*a*), and typical (de-noised) raw traces are presented in figure 15(*b*). Three wake-passing periods have been plotted, and the streamwise positions of each hot-film sensor have been indicated by the dots along the top of each diagram. The paths of the wake centreline and the maximum and minimum $\langle U_{fs} \rangle$ have been duplicated from figure 13(*b*). The measured quasi-wall shear stress drops sharply as

https://doi.org/10.1017/jfm.2011.204 Published online by Cambridge University Press

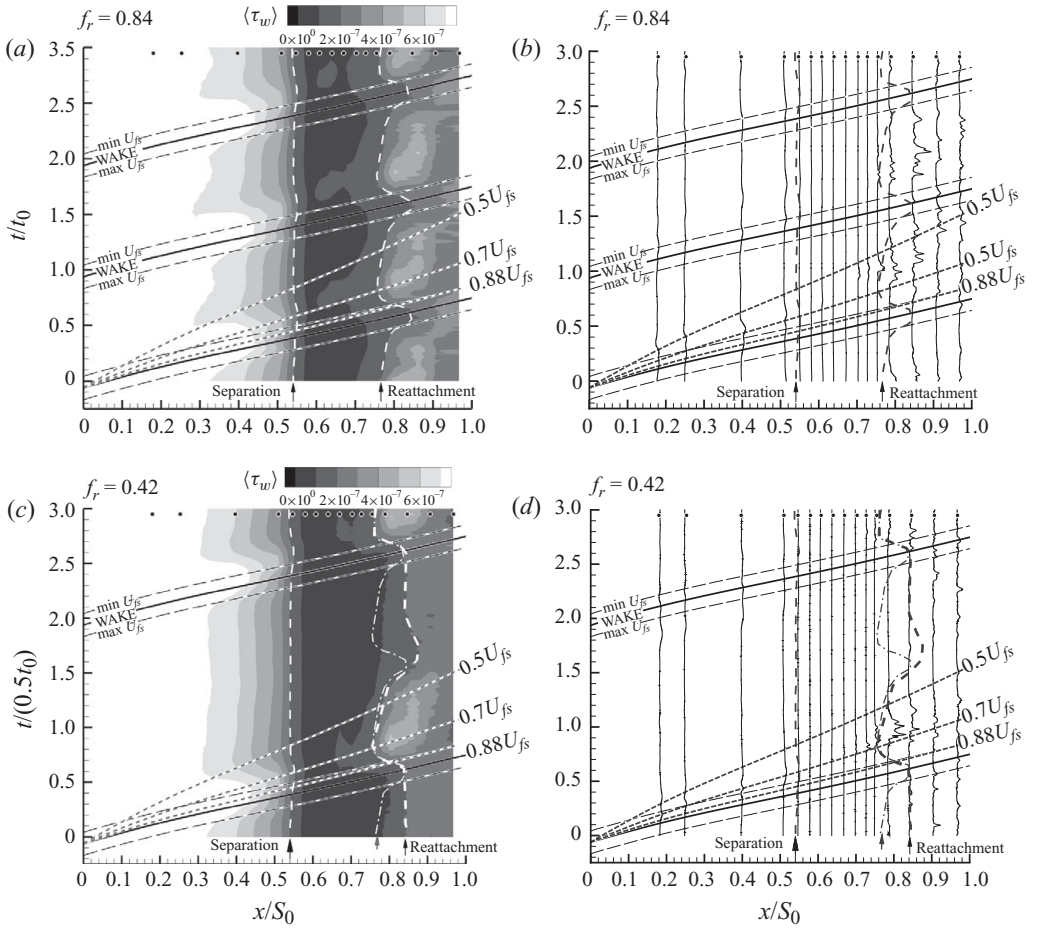


FIGURE 15. Unsteady hot-film data at two wake frequencies. (*a*, *c*) Contours of phase-averaged quasi-wall shear stress; (*b*, *d*) Raw traces. Dash-dotted lines in (*c*) and (*d*) show unsteady reattachment at higher wave frequency.

the free-stream flow decelerates (downstream of $x/S_0 = 0.42$), reaching low values in the separation bubble and remaining low until flow reattachment. It should be noted that the quasi-shear stress does not drop to zero because the flow is inherently unsteady. At separation and re-attachment, the mean wall shear stress is zero, but its instantaneous value will fluctuate between positive and negative shear. The hot-film sensors are not sensitive to direction, so a positive value of quasi-wall shear stress will be recorded at both locations. Estimates of the phase-averaged separation and reattachment locations have been included in figure 15 by indicating where the contours, respectively, fall below and rise above a value of 2×10^{-7}. This value is arbitrary. It is chosen based on experience and it matches the steady separation location observed with flow visualisation. This method of determining separation and re-attachment locations is approximate, but it is sufficient to illustrate the temporal variation of these parameters. The estimated separation location varies only slightly through the wake cycle (with a peak-to-peak fluctuation of approximately $0.01\,S_0$) while the re-attachment location varies significantly (by about $0.08\,S_0$). Inside the bubble, the raw traces in figure 15(*b*) show almost no fluctuations, consistent with

https://doi.org/10.1017/jfm.2011.204 Published online by Cambridge University Press

almost stagnant flow. Downstream of the reattachment line, the raw traces contain fluctuations that are indicative of turbulent attached flow.

The data in figure 15(*a*) demonstrate that at a reduced frequency $f_r = 0.84$, the separation bubble does not reach a steady-state between each wake passing. Consequently, the influence of each wake cannot be entirely separated from that of its predecessor. In order to clarify the results, figures 15(*c*) and 15(*d*) show hot-film data obtained at a lower wake frequency ($f_r = 0.42$), which was achieved by removing every other bar from the moving belt. Note that the wake period t_0 has doubled relative to figure 15(*a*): to ensure that the time axes are identical to the $f_r = 0.84$ case, the vertical axes in figures 15(*c*) and 15(*d*) show $t/(0.5t_0)$ rather than t/t_0. At this lower reduced frequency, the boundary layer has longer to recover between wakes, so the influence of each wake can effectively be observed in isolation. The bubble reaches an approximately steady size during the interval $t/(0.5t_0) \approx 0 \rightarrow 0.25$, prior to the wake's arrival over the separation bubble. As the wake convects over the front of the bubble ($t/(0.5t_0) \approx 0.25 \rightarrow 0.5$), it has little apparent effect on the re-attachment location. In fact, the size of the bubble remains almost unchanged until the wake centreline passes over the reattachment location ($t/(0.5t_0) \approx 0.6$). After this time, wake-induced transition is evident and the bubble shortens significantly, reaching a minimum length at around $t/(0.5t_0) = 0.75$. The bubble remains shorter than its steady length until $t/(0.5t_0) \approx 1.4$, a delay of $0.8\,(0.5t_0)$ after the wake centreline has passed over the reattachment location. After this time, the reattachment location moves further aft, so that the bubble becomes slightly longer than its steady flow length. This effect can be explained if a 'calmed' flow region follows behind the wake-induced turbulence. Such calmed regions are observed at the trailing edge of classical Emmons turbulent spots and have been previously identified in studies of wake-induced transition (e.g. Pfeil, Herbst & Schröder 1982). Finally, the bubble returns to a quasi-steady state at around $t/(0.5t_0) = 2$, and the cycle repeats itself.

The re-attachment lines for both wake frequencies are shown in figure 15(*c*); by comparing these lines, it can be observed that the re-attachment line at the higher reduced frequency is simply a superposition of the quasi-isolated wake effects observed at the lower wake frequency. For $f_r = 0.84$ (figure 15*c*), the re-attachment location is in the process of moving aft as the next wake arrives ($t/(0.5t_0) \approx 1.5$). The late re-attachment observed directly under the wake path in figure 15(*a*) is therefore caused by the calmed region induced by the preceding wake.

Clearly, any understanding of the transition process must account for the fact that the wake-induced transition persists for some time ($\sim 0.8\,t_0$, figure 15*a*) after the wake centreline has passed. This delay cannot be satisfactorily explained simply by the width of the wake: the trailing edge of the wake trails behind the centreline by only $0.35\,t_0$ (figures 13 and 14). The delay can be explained if the wake induces disturbances close to the flat-plate leading edge, which convect downstream more slowly than the wake. Three additional lines have been included in the plots of figure 15 to show the convection of disturbances from the leading edge at 88%, 70% and 50% of the free-stream velocity. These are the approximate convection rates of a turbulent spot leading and trailing edge in zero pressure gradient. Strictly speaking, the celerities in figure 15 should be modified to account for the effects of the local streamwise pressure gradients on the celerity. However, these approximate values are sufficiently accurate for the purposes of the current discussion. The early re-attachment induced by the wake is approximately bounded by the 88% and 50% paths. The earliest re-attachment is observed along the $0.7\,U_{fs}$ path, suggesting that the strongest wake-induced disturbances travel at this celerity. Similar propagation

https://doi.org/10.1017/jfm.2011.204 Published online by Cambridge University Press

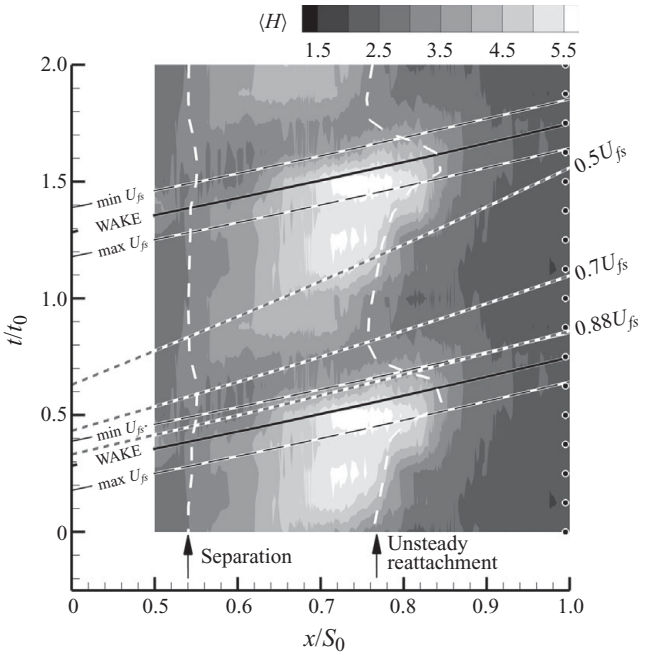


FIGURE 16. Phase-averaged shape factor $H = \delta * /\theta$ calculated from the PIV data along the flat-plate mid-span.

rates have been identified in previous studies, most notably the flat-plate experiments of Orth (1993). The $0.7\,U_{fs}$ celerity rate is also strongly evident in experimental studies of wake-induced transition in compressors (e.g. Solomon, Walker & Hughes 1999; Wheeler, Sofia & Miller 2007). The instantaneous data will demonstrate that these wake-induced disturbances are in fact amplified Klebanoff streaks, similar to those observed by Wu *et al.* (figure 4).

3.2.3. *Boundary-layer parameters*

The unsteady boundary-layer parameters have been calculated from the phase-averaged PIV measurements along the flat-plate mid-span. Figure 16 shows the variation through the wake cycle of the shape factor H, which is the ratio of the displacement thickness to the momentum thickness. The estimated uncertainty in this parameter is ± 0.3, which arises from the errors in the velocity vectors (figure 11) and the relatively low spatial resolution of the PIV data. The unsteady separation and re-attachment lines in figure 16 have been duplicated from figure 15. At separation $H \approx 3$, in line with previous investigations on LP turbine blades (e.g. Stieger & Hodson 2004; Zhang, Hodson & Harvey 2005). The shape factor in the bubble is strongly periodic. The maximum value ($H \approx 5.5$) is observed at around $t/t_0 \approx 0.4$. The hot-film data in figure 15 demonstrated that the bubble grows in size during this phase as the influence of the previous wake fades. Between the $0.88\,U_{fs}$ and $0.5\,U_{fs}$ trajectories, figure 16 shows that the bubble exhibits low values of H during these periods. This observation coincides with the early wake-induced transition observed in figure 15.

Figure 17 shows a space–time plot of the momentum thickness θ through the wake cycle. The estimated error in this parameter is $\pm 0.0005\,S_0$. The plot shows a distinct region of elevated momentum thickness which approximately follows the $0.7\,U_{fs}$ trajectory, and therefore the wake-amplified Klebanoff streaks. This region of

https://doi.org/10.1017/jfm.2011.204 Published online by Cambridge University Press

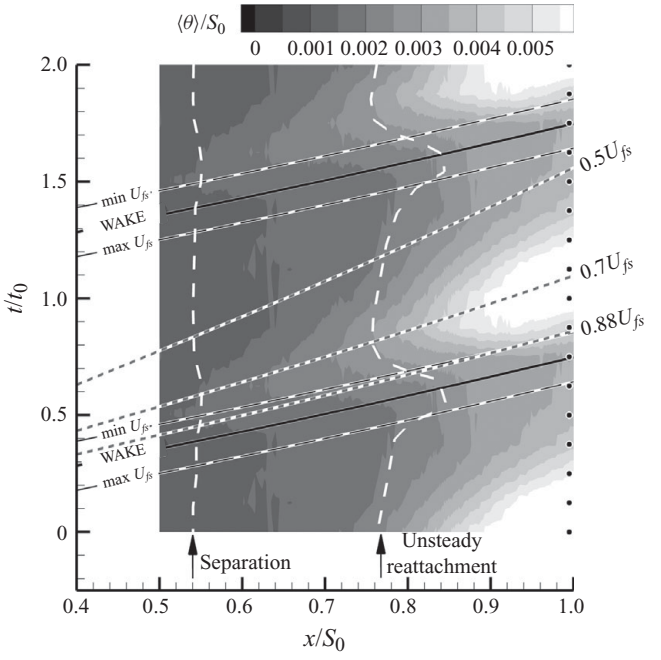


FIGURE 17. Phase-averaged momentum thickness calculated from the PIV data along the flat-plate midspan.

elevated momentum thickness increases the profile loss of the LP turbine (Coull & Hodson 2010), and therefore its origin is of significant practical concern.

4. Instantaneous measurements

This section examines the roles of the wake-induced Klebanoff streaks (associated with the $0.5\,U_{fs}$, $0.7\,U_{fs}$ and $0.88\,U_{fs}$ celerity rates) and the KH instability in the transition process.

4.1. *Klebanoff streaks in the boundary layer*

4.1.1. *Weak Klebanoff streaks induced by the free-stream turbulence in steady flow*

In steady flow, the background turbulence generated by the upstream grid induces relatively weak Klebanoff streaks in the boundary layer, which are evident in the wall-parallel PIV data. Such structures can be visualised by plotting the wall-normal vorticity, which is non-dimensionalised by the reference length and velocity

$$\omega* = (S_0/U_{TE})(\mathrm{d}U_x/\mathrm{d}z - \mathrm{d}U_z/\mathrm{d}x). \tag{4.1}$$

Figure 18 shows an example of an instantaneous wall-parallel measurement for steady flow from measurement plane 1. As figure 11(*a*) shows, this plane lies above the edge of the boundary layer for $x/S_0 < 0.65$ and in the outer region of the boundary layer for $x/S_0 > 0.65$. It is in this outer region of the boundary layer that one might expect to observe local breakdown to turbulent flow, as noted by Wu *et al.* (1999) for wake-induced transition and Jacobs & Durbin (2001) for bypass transition. Contours of the dimensionless wall-normal vorticity $\omega*$ are presented in figure 18(*a*), which reveals the presence of streamwise streaks in the boundary layer. The apparent growth of these streaks in the streamwise direction is largely due to the variation

https://doi.org/10.1017/jfm.2011.204 Published online by Cambridge University Press

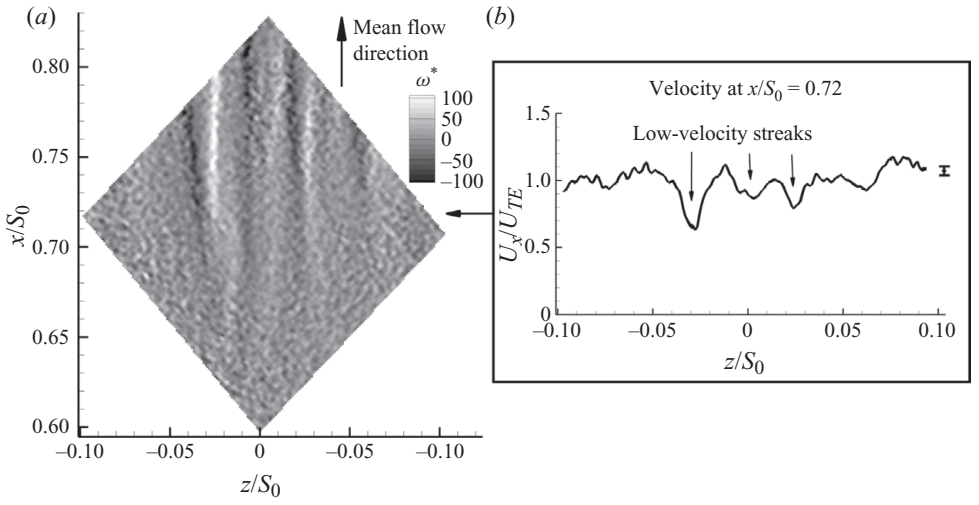


FIGURE 18. Instantaneous data for steady flow, $y/S_0 = 0.014$ (plane 1 in figure 11*a*): (*a*) contours of wall-normal vorticity; (*b*) streamwise velocity across the span.

in the boundary-layer thickness (figure 11). The variation of U_x across the span at $x/S_0 = 0.72$ is shown in figure 18(*b*), and shows that the streaks have lower velocity than the surrounding fluid. These streaks are therefore Klebanoff streaks induced by the elevated free-stream turbulence. Although variation is observed between individual data, this example is typical of most of the instantaneous measurements in steady flow. It should be noted that the spanwise spacing of the streaks is around 0.02–$0.03S_0$. This is similar to the wavelength observed in the phase-averaged data in figure 12, and is close to the streak spacing observed by Matsubara & Alfredsson 2001.

4.1.2. *Strong Klepbanoff streaks induced by the wake turbulence*

As each wake passes over the leading edge, the elevated turbulence level generates a region of stronger Klebanoff streaks which propagates downstream. The example labelled as case 3 in figure 19 shows a typical example at a phase of $t/t_0 = 0.625$, as the region of minimum free-stream velocity induced by the wake passes over the bubble (indicated in the plot). The data are presented in the same manner as in figure 18. The streaks in case 3 of figure 19 have a larger velocity deficit compared to the steady flow example in figure 18 and exhibit higher levels of wall-normal vorticity.

Durbin *et al.* (2009) demonstrated that Λ-vortices can emerge from the interaction of the Klebanoff streaks with the inherent instability of the boundary layer (process *b* in figure 3). While it is difficult to identify such three dimensional structures from the planar PIV data, there is evidence to suggest that a similar process is underway. Case 4 in figure 19 shows an instantaneous measurement from a slightly later phase ($t/t_0 = 0.750$) than case 3. The streak centred along $z/S_0 \approx -0.03$ has very low velocity along its centre. This perturbation is far higher than previously observed for Klebanoff streaks: Jacobs & Durbin (2001) and Alfredsson & Matsubara (1996) noted perturbations of around 25% of the free-stream velocity. This result therefore suggests that these strong perturbations may correspond to the slow moving flow between the two legs of a Λ-vortex, in line with the simulations of Durbin *et al.* (2009). These large fluctuations could also indicate varicose streak instability, as visualised by Asai, Minagawa & Nishioka (2002). The strong streak in case 4 of figure 19 (centred on $z/S_0 \approx -0.03$) shows that the streak becomes increasingly

https://doi.org/10.1017/jfm.2011.204 Published online by Cambridge University Press

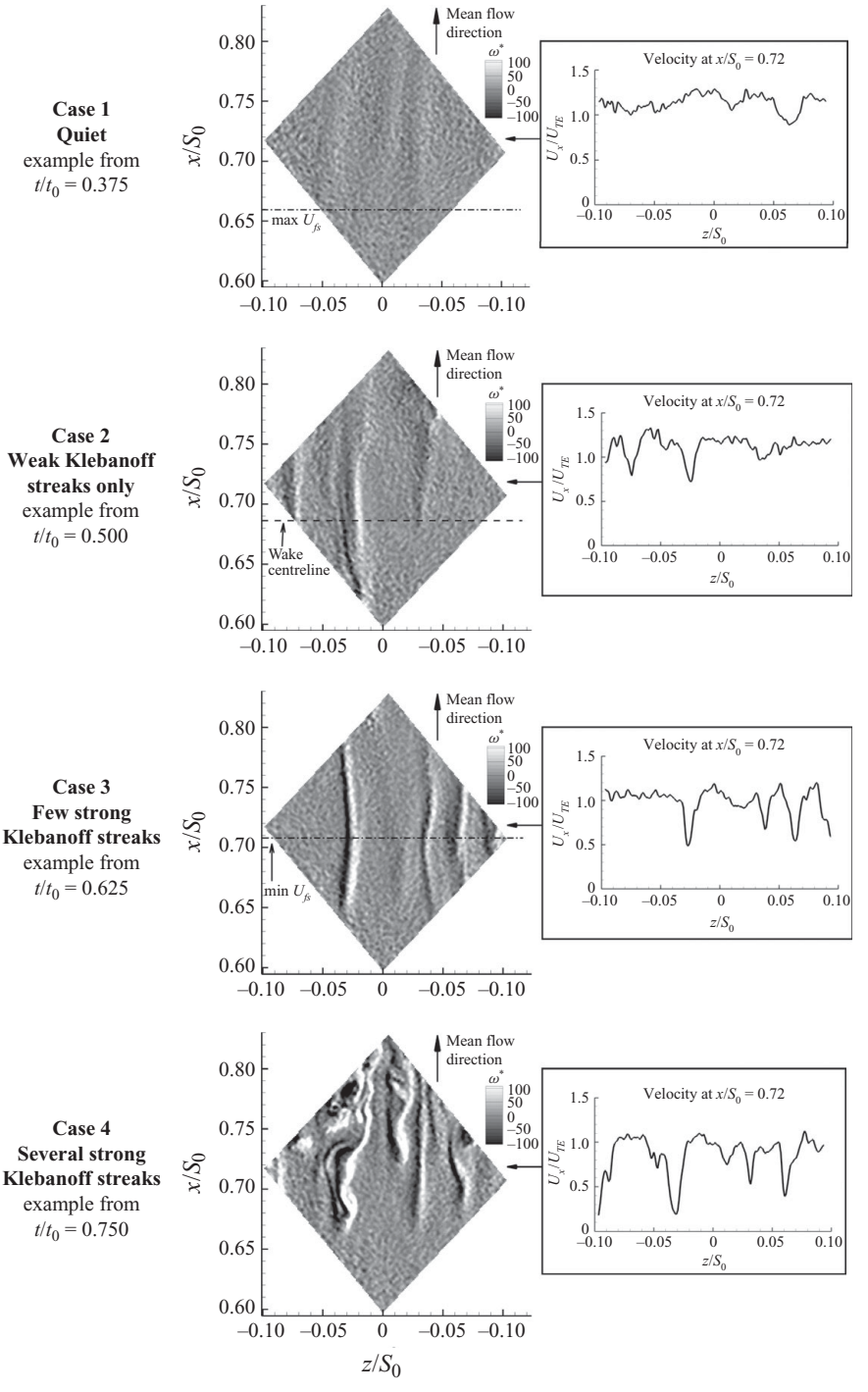


FIGURE 19. Examples of instantaneous wall-normal vorticity for unsteady flow, $f_r = 0.84$, $y/S_0 = 0.014$ (measurement plane 1 in figure 11*a*). Case 1 (quiet) example from $t/t_0 = 0.375$, case 2 (weak Klebanoff streaks only) example from $t/t_0 = 0.500$, case 3 (few strong Klebanoff streaks) example from $t/t_0 = 0.625$, case 4 (several strong Klebanoff streaks) example from $t/t_0 = 0.750$.

https://doi.org/10.1017/jfm.2011.204 Published online by Cambridge University Press

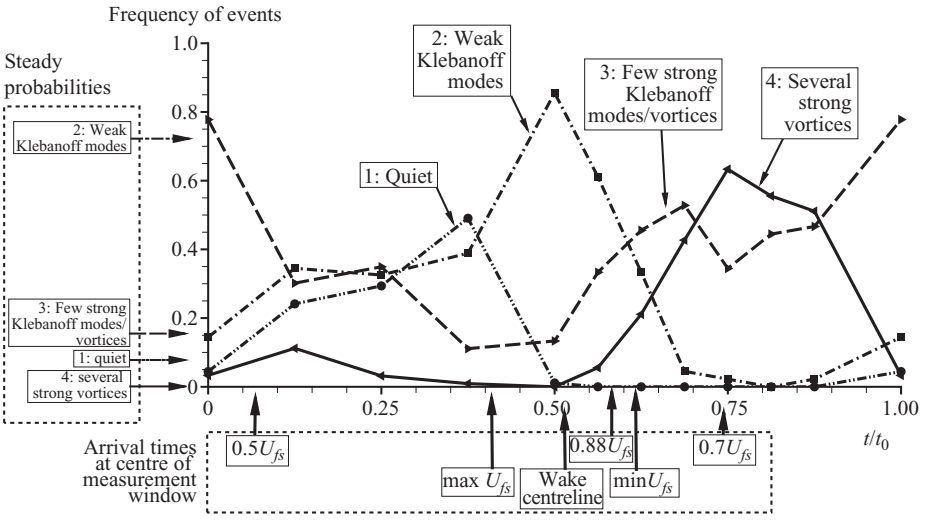


FIGURE 20. Estimated frequencies of the four cases shown in figure 19; comparison of steady and unsteady flow behaviour, $f_r = 0.84$.

distorted further downstream, before breaking down into a series of smaller vortices ($x/S_0 > 0.75$) of varying scale, which is indicative of breakdown to turbulent flow.

4.1.3. *Variation through the wake cycle*

The instantaneous examples discussed above provide little information about the variation in the flow behaviour through the wake cycle. To present this information, a statistical approach has been applied by categorising the measurements at each phase in the wake cycle. Figure 19 shows four examples of instantaneous data from wall-parallel measurement plane 1 (figure 11*a*), presented in the same manner as in figure 18. As indicated, the four cases have been obtained at various stages in the wake cycle and represent the most likely flow behaviour at these phases. Significant variation between individual measurements was observed, but, in general, all of the instantaneous measurements were similar to one of the cases marked in figure 19 as follows.

Case 1 – *Quiet*. The data exhibit very low levels of vorticity across the measurement window, with no strong evidence of Klebanoff streaks.

Case 2 – *Weak Klebanoff streaks only*. The data exhibit relatively weak Klebanoff streaks, with low vorticity levels ($|\omega*| < 75$) throughout the measurement window.

Case 3 – *Few strong Klebanoff streaks/vortices*. The data exhibit one or two structures with high levels of vorticity ($|\omega*| > 75$), many of which appear to indicate Λ-vortices. Some of these vortices are irregular in structure.

Case 4 – *Several strong Klebanoff streaks/vortices*. The data exhibit three or more structures with high levels of vorticity ($|\omega*| > 75$), which are often irregular in structure, as the example in figure 19 shows.

The data were manually categorised into cases 1–4 for both steady flow and for each time-step through the wake cycle, allowing the probability of each to be estimated. This information is presented in table 2 alongside general observations of the flow behaviour. The results are also plotted in figure 20 alongside the time of arrival of the wake front, centreline and rear at the approximate centre of the measurement window ($x/S_0 = 0.70$). These arrival times may be used to compare figure 20 with the space–time diagrams in figures 13–17. The arrival of the $0.88\,U_{fs}$, $0.7\,U_{fs}$ and $0.5\,U_{fs}$ trajectories have also been indicated.

https://doi.org/10.1017/jfm.2011.204 Published online by Cambridge University Press

t/t_0	Case 1 Quiet	Case 2 Weak Klebanoff streaks only	Case 3 Few strong Klebanoff streaks	Case 4 Several strong Klebanoff streaks/vortices	Observations
Steady flow	0.09	0.75	0.15	0.00	Frequent occurrence of weak streaks, occasional isolated strong streak
0.125	0.24	0.34	0.30	0.11	Few weak streaks; similar to steady but quieter
0.250	0.29	0.33	0.35	0.03	Few weak streaks; similar to steady but quieter
0.375	0.49	0.39	0.11	0.01	Few weak streaks; similar to steady but quieter
0.500	0.01	0.86	0.13	0.00	Many weak streaks; a few stronger streaks
0.5625	0.00	0.61	0.33	0.06	More strong streaks but little sign of breakdown
0.625	0.00	0.33	0.46	0.21	Stronger streaks, evidence of distortion and breakdown
0.6875	0.00	0.04	0.53	0.43	Many strong streaks, many highly distorted
0.750	0.00	0.02	0.34	0.63	Increasing number of strong streaks and flow structures with irregular structure
0.8125	0.00	0.00	0.44	0.56	Many irregular flow structures and strong streaks
0.875	0.00	0.02	0.47	0.51	Many irregular flow structures and strong streaks
1.000	0.04	0.14	0.78	0.03	Few weak streaks; much quieter; isolated irregular flow structures

TABLE 2. Estimated frequencies of the four cases shown in figure 19; comparison of steady and unsteady flow behaviour, $f_r = 0.84$.

In steady flow, the vast majority of the measurements (75%) revealed weak Klebanoff streaks (case 2) induced by the background turbulence, as observed in figure 18. To aid the description of the unsteady flow behaviour, examples of instantaneous measurements obtained during the wake interaction have been plotted in figure 21. The approximate positions of the front, rear and centreline of the wake have been indicated on these plots. Together with the statistical information in table 2 and figure 20, the flow behaviour through the wake cycle is as follows.

Phase period $t/t_0 = 0.125$–0.375. The instantaneous measurements show a higher frequency of case 3 (strong vortices) than in steady flow, a result which concurs with the hot-film data (figures 15*a* and 15*b*) which show early wake-induced transition during these phases. The hot-film data also show that the re-attachment location moves aft for $t/t_0 = 0.125$–0.375 under the influence of a calmed flow region following the wake-induced turbulence. Figure 20 shows that the frequency of strong vortices (case 3) diminishes during this time, while the frequency of quiet measurements (case 1)

https://doi.org/10.1017/jfm.2011.204 Published online by Cambridge University Press

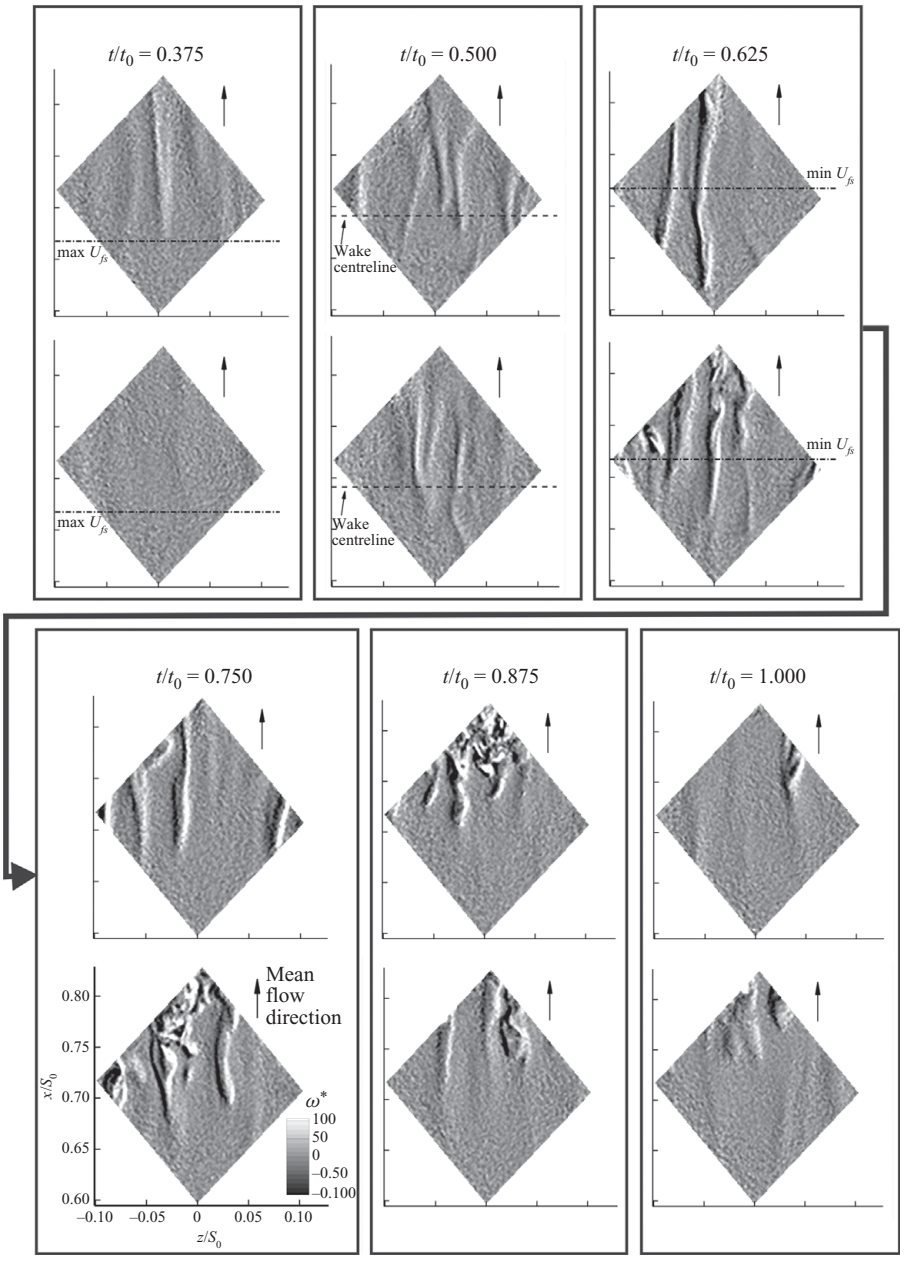


FIGURE 21. Examples of instantaneous measurements through the wake cycle: contours of normalised vorticity, $f_r = 0.84$, $y/S_0 = 0.014$ (plane 1 in figure 11a). For each time-step, two representative (but unrelated) examples are shown.

rises. In some part, the frequent occurrence of quiet measurements can be explained by the thinning of the boundary layer during these phases. Figure 22(a) shows the relative position of measurement plane 1 and the boundary-layer edge. However, the boundary-layer thinning is not wholly responsible for the trends observed in figure 20. During the interval $t/t_0 = 0.125$–0.375, figure 22(a) shows that the boundary layer thickens over most of the surface ($0.66 < x/S_0 < 0.77$), while the frequency of quiet

https://doi.org/10.1017/jfm.2011.204 Published online by Cambridge University Press

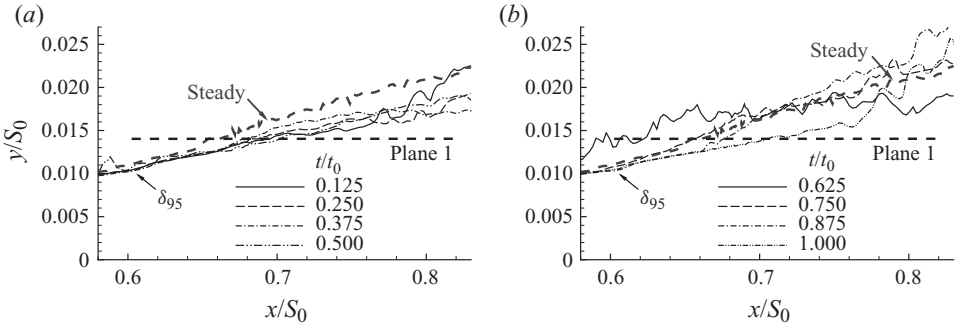


FIGURE 22. The relative height of measurement plane 1 in the boundary layer at each phase in the wake cycle: (*a*) $t/t_0 = 0.125$–0.500; (*b*) $t/t_0 = 0.625$–1.000.

measurements (case 1 in figure 20) increases substantially. In addition, data obtained at lower heights in the boundary layer (not presented) frequently show quiet flow behaviour during these phases. The high frequency of the quiet periods must therefore be caused by the flow calming effect which causes the late re-attachment observed in figure 15(*b*). The timing in figure 20 is consistent with this conclusion.

Phase $t/t_0 = 0.500$. As the wake centreline convects over the separation bubble, table 2 and figures 20 and 21 show a large number of weak Klebanoff streaks, which are predominantly straight with little evidence of distortion.

Phase period $t/t_0 = 0.5625$–0.6875. As the region of minimum free-stream velocity induced by the wake passes over the bubble, an increasing number of strong Klebanoff streaks are observed (case 3). The phase $t/t_0 = 0.5625$ approximately corresponds to the arrival of the first wake-amplified Klebanoff streaks at the centre of the measurement window (along $0.88\,U_{fs}$ path). A significant proportion of the streaks are distorted, as shown in the example in the bottom plot of figure 21 for $t/t_0 = 0.625$.

Phase period $t/t_0 = 0.750$–0.8125. Some time after the wake has convected past the separation bubble, strong streaks persist in the boundary layer. As figure 20 shows, the most frequent occurrence of case 4 (several strong Klebanoff streaks/vortices) occurs at $t/t_0 = 0.750$. This phase coincides with the arrival of wake-amplified Klebanoff streaks from the leading edge with a convection velocity of $0.7\,U_{fs}$ (figures 15–17). A large proportion of the streaks observed at these time-steps are highly distorted, as in the bottom plot of figure 21 for $t/t_0 = 0.750$, suggesting that Λ-vortex formation and localised turbulent breakdown are underway.

Phase $t/t_0 = 0.875$. During this phase, fewer streaks are observed. The two plots in figure 21 show that the early portion of the boundary layer ($x/S_0 < 0.70$) is now quiet. This effect appears to be largely due to thinning of the boundary layer in this region during this phase (figure 22*b*). Distorted flow structures, exhibiting high levels of vorticity, are observed in the downstream portion of the boundary layer ($x/S_0 > 0.70$). This is indicative of predominantly turbulent flow in this region.

Phase $t/t_0 = 1.000$. Less activity is observed in the boundary layer as the bubble starts to return towards its steady flow behaviour. Some flow structures (exhibiting relatively high levels of vorticity) are visible in the downstream portion of the boundary layer in figure 21 ($x/S_0 > 0.74$) but there are fewer of them. Upstream of $x/S_0 = 0.74$, the boundary layer appears almost quiet. This location approximately corresponds to the trailing edge of the wake-amplified Klebanoff streaks (the $0.5\,U_{fs}$ line in figures 15–17), but the effect is also due to the thinning of the boundary layer during this phase, evident in figure 22(*b*).

https://doi.org/10.1017/jfm.2011.204 Published online by Cambridge University Press

Together with the phase-averaged results, the instantaneous data show that the wake generates a region of amplified Klebanoff streaks close to the leading edge, via a shear-sheltering receptivity process that is similar to that which occurs in steady bypass transition (process *a* in figure 3). The region of wake-amplified Klebanoff streaks convects downstream at a fraction of the free-stream velocity, spreading as it does so. The leading and trailing edges of this region travel at similar velocities as a classical turbulent spot, at approximately $0.5\,U_{fs}$ and $0.88\,U_{fs}$ respectively; a result which is consistent with the simulation of Wu *et al.* (1999) presented in figure 4. The strongest streaks travel at approximately 70% of the free-stream velocity, and induce the earliest re-attachment of the bubble (figure 15). The streaks undergo distortion and localised breakdown to turbulent flow, arguably via the production and breakdown of lambda-vortices (processes *b* and *c* in figure 3). Behind the region of wake-amplified Klebanoff streaks, a region of calmed flow is observed, similar to that observed at the trailing edge of classical turbulent spots. The calming effect acts to delay transition and thus the bubble re-attachment (as evident in figure 15*b*).

4.2. *The role of the inflectional (KH) instability*

In the previous section, data were presented from measurement plane 1 which indicated the presence of Klebanoff streaks convecting into the separation bubble from upstream. McAuliffe & Yaras (2010) demonstrated that such streaks will distort the separated shear layer, making it highly three-dimensional. Their simulations showed that the formation of spanwise-coherent KH vortices by the global instability of the shear layer was suppressed by the streaks. However, KH-type instability with a similar wavelength was evident in localised regions of the shear layer. Similar behaviour is evident in the current measurements, as shall be examined in this section. Data are presented from measurement plane 2, which is located further downstream than measurement plane 1 (figure 11*a*).

Inviscid Rayleigh stability analysis has been performed on the steady mid-span velocity profiles shown in figure 11(*a*), using a code provided by O. N. Ramesh and S. S. Diwan of the Indian Institute of Science. This approach is more straightforward than solving the full Orr–Sommerfeld stability equation, and for separated flows it gives good predictions of the most amplified disturbance (Diwan & Ramesh 2009). A smooth spline curve was fitted to the relatively sparse PIV velocity data in order to obtain smooth differentials, an example of which is shown in figure 11(*b*). The predicted frequency and wavelength of the most amplified disturbance are presented in non-dimensional form in figures 23(*a*) and 23(*b*), respectively. There is clearly some degree of scatter on these plots due to the velocity uncertainties and relatively poor spatial resolution of the data (figure 11). Nonetheless, the analysis clearly predicts an instability wavelength of about $\lambda_{KH}/S_0 \approx 0.065$ and a frequency of $f_{KH}S_0/U_{TE} \approx 7.5$. Upstream of $x/S_0 = 0.6$, the code failed to converge because of the small number of data points in the boundary layer and the resultant poor spline fit.

In unsteady flow, the boundary layer profiles vary through the wake cycle, and so the most amplified disturbances will deviate slightly from the steady predictions in figure 23. In particular, the boundary layer is thinner during most of the wake cycle compared to steady flow (figure 22), which will tend to favour the amplification of higher frequency/lower wavelength disturbances. It should also be noted that Rayleigh stability analysis tends to predict a sharp peak in the frequency response that is absent in measurements (e.g. Yarusevych, Kawall & Sullivan 2008). One would therefore expect to observe disturbances at a range of wavelengths rather than a distinct wavelength and, indeed, the data demonstrate this.

https://doi.org/10.1017/jfm.2011.204 Published online by Cambridge University Press

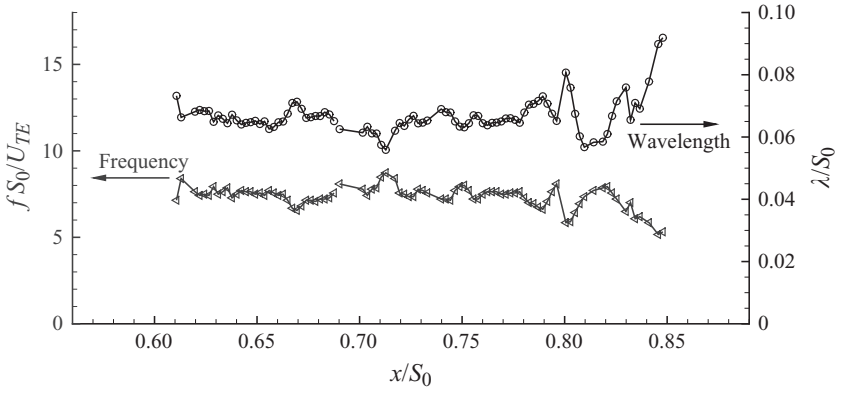


FIGURE 23. Most amplified frequency and wavelength through the separation bubble, from Rayleigh stability analysis.

The measurements parallel to the wall were obtained using stereoscopic PIV, which allows the wall-normal velocity U_y to be measured. This component of velocity can be used to examine the spatial nature of the KH disturbances in the shear layer. In the case of two-dimensional KH disturbances, one would expect to observe alternate spanwise regions of positive disturbance velocity (away from the wall) and negative disturbance velocity (towards the wall) spaced at half of the KH wavelength in the direction of the flow. However, the flow behaviour is more complex than this simple case, as a result of the unsteady flow environment and the streaky Klebanoff streaks present in the boundary layer.

Four examples of instantaneous measurements from measurement plane 2 (figure 11*a*) are shown in figure 24 for unsteady flow. For consistency, the data have been obtained at the same phases as for the streaks in figure 19, but in figure 24 the examples do not necessarily represent the most frequently observed flow behaviour at each phase. In the left-hand column, the wall-normal vorticity has been plotted for each measurement; the central column shows the wall-normal velocity U_y/U_{TE}; and to the right, the two-dimensional spatial autocorrelation of U_y/U_{TE} has been presented

$$R_{2D}\left(x_{shift}, z_{shift}\right) = \frac{\overline{U_y(x,z) \times U_y(x + x_{shift}, z + z_{shift})}}{U_{TE}^2}. \tag{4.2}$$

This autocorrelation could be applied to the disturbance velocities ($U_y' = U_y - \langle U_y \rangle$), but, in practice, it makes very little difference since the variations in instantaneous velocity U_y are much higher than those in the phase-averaged $\langle U_y \rangle$. The numerator of the autocorrelation in (4.2) is averaged over the range of x and z for which both (x, z) and $(x + x_{shift}, z + z_{shift})$ are contained within the measurement window. The autocorrelation may be used to identify distinct streamwise and spanwise wavelengths in the flow field, indicated by a peak in the two-dimensional autocorrelation map.

Significant variation is observed between individual measurements, but they can be manually categorised by the KH disturbances (or lack thereof) evident in the autocorrelation maps and the contour plots of U_y. KH structures were detected when the first streamwise peak of the autocorrelation function was in the range 0.04–0.07S_0, an interval which reflects the thinning of the boundary layer in unsteady flow. The recorded flow fields are generally similar to one of the four examples labelled in figure 24 as follows.

https://doi.org/10.1017/jfm.2011.204 Published online by Cambridge University Press

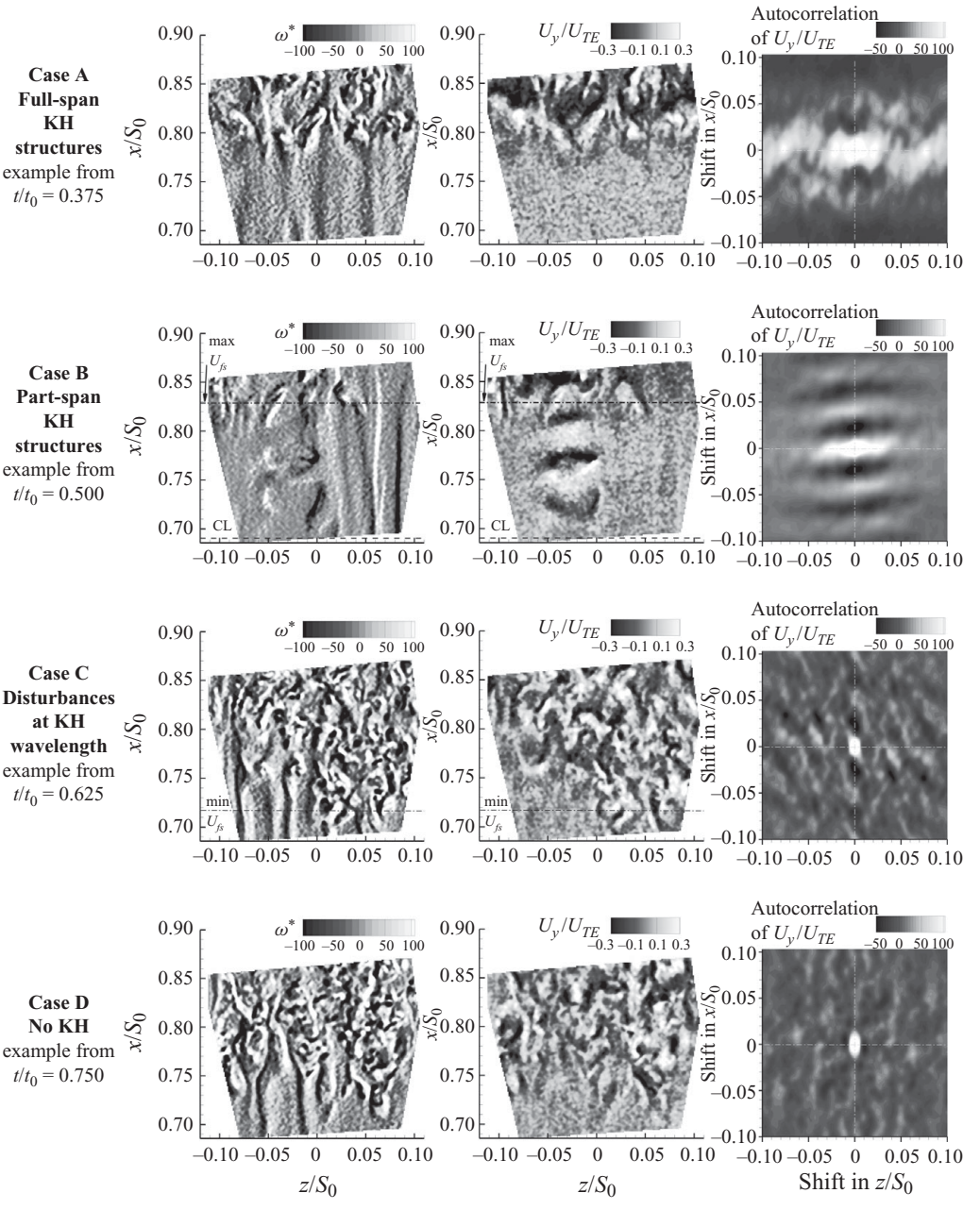


FIGURE 24. Four examples of instantaneous normalised wall-normal velocity and wall-normal vorticity for steady flow, $y/S_0 = 0.011$ (plane 2 in figure 11*a*). Case A (Full-span KH structures) example from $t/t_0 = 0.375$, case B (Part–span KH structures) example from $t/t_0 = 0.500$, case C (Disturbances at KH wavelength) example from $t/t_0 = 0.625$, case D (No KH) example from $t/t_0 = 0.750$.

Case A – Full-span KH structures. A structure with a streamwise wavelength close to the predicted KH wavelength is observed to stretch across the measurement domain (central plot). Along the centreline of the autocorrelation plot ($z_{shift} = 0$), peaks are visible at $x_{shift} \approx \pm 0.05$, close to the wavelength predicted by the stability analysis

https://doi.org/10.1017/jfm.2011.204 Published online by Cambridge University Press

(figure 23). Although the KH disturbances stretch across the full measurement domain, they are not coherent in the spanwise direction: rather the large-scale KH structure is distorted by a number of small-scale disturbances, which are also evident in the vorticity plot on the left-hand side for $x/S_0 > 0.8$. This plot also shows that the Klebanoff streaks induced by the background turbulence ($x/S_0 < 0.8$) are relatively weak during this phase, in line with the observations in the previous section (e.g. figure 21).

Case B – Part-span KH structures. Structures are observed which have a similar streamwise spacing to the predicted KH wavelength, but which cover only a portion of the measurement window span ($>0.02S_0$) rather than the full width. In this particular case, a structure is evident in the central plot for $-0.05 < z/S_0 < 0$, and can be seen to exhibit four peaks and troughs in the wall-normal velocity. The autocorrelation plot indicates a streamwise periodicity with a wavelength close to the predicted KH wavelength. The vorticity plot for case B is similar to that for case A, showing weak Klebanoff streaks for $x/S_0 < 0.8$ and small-scale fluctuations for $x/S_0 > 0.8$. It should be noted that not all of the measurements exhibiting part–span KH structures showed as many peaks and troughs as the example in figure 24.

Case C – Disturbances at the KH-wavelength. In this case, the plot of U_y does not exhibit any clear KH-wavelength structures, and instead indicates many small-scale fluctuations in the flow. Nevertheless, there is a clear tendency for disturbances to occur at a streamwise wavelength close to the KH wavelength, as demonstrated by the periodicity in the autocorrelation plot along the centreline ($z/S_0 = 0$). The presence of the KH wavelength in the small-scale fluctuations indicates that case C shows the early stages of KH vortex breakdown. The autocorrelation plot also suggests that there is a dominant spanwise wavelength of around 0.02–0.03 S_0 (along the $x/S_0 = 0$ line). This wavelength corresponds to the spacing of Klebanoff streaks. The vorticity plot shows the presence of strong wake-amplified streaks in the shear layer.

Case D – No KH-wavelength disturbances. Again, only small-scale fluctuations are visible in the wall-normal velocity U_y, but in this case the autocorrelation plot on the right-hand side does not reveal a streamwise wavelength close to the predicted KH value. This case therefore displays a more complete turbulent breakdown of the flow than in case C above. As for case C, the vorticity plot shows the presence of strong wake-amplified Klebanoff streaks.

The measurements have been categorised in this manner for steady flow and through the unsteady wake cycle. The estimated frequencies of cases A–D are presented in table 3, alongside observations of the flow behaviour. The frequencies have also been plotted in figure 25. In general, the unsteady flow data tended to show less spanwise coherence than the steady measurements, as indicated by the relatively low probability of case A through the entire wake cycle in the unsteady data. One may therefore conclude that the bubble does not reach a quasi-steady state between wakes. In addition, most of the part–span KH structures in steady flow consisted only of one or two peaks and troughs. The unsteady flow demonstrated significantly less spanwise coherence than the steady flow measurements, and far fewer full-span KH structures (case A) were observed. The variation through the phases of the wake cycle is described below with examples of the key observations.

Phase period $t/t_0 = 0.125$–0.250. Prior to the wake arrival, the observed measurements are similar to the steady flow case, but less spanwise coherence is observed (low probability of cases A and B). The KH structures also tend to be shorter in the spanwise direction than for steady flow.

https://doi.org/10.1017/jfm.2011.204 Published online by Cambridge University Press

t/t_0	Case A Full-span KH	Case B Part-span KH disturbances	Case C Disturbances at KH wavelength	Case D No KH	Observations
Steady flow	0.13	0.14	0.59	0.14	Quiet upstream of $x/S_0 = 0.8$; usually only 1 or 2 peaks and troughs at KH wavelength; large-scale rather than small-scale variation
0.125	0.02	0.08	0.55	0.34	Similar to steady but with less spanwise coherence of structures
0.250	0.02	0.08	0.46	0.44	Similar to steady but with less spanwise coherence of structures
0.375	0.07	0.10	0.31	0.51	Many quiet cases with no KH; very occasional short-span KH structures
0.500	0.00	0.35	0.32	0.33	Several short-span KH structures originating at $x/S_0 < 0.7$; otherwise quiet for $x/S_0 < 0.8$
0.5625	0.00	0.46	0.41	0.13	More activity further upstream; many short-span KH structures
0.625	0.00	0.19	0.61	0.20	Fewer and less coherent KH structures; more small-scale activity with λ_{KH}
0.6875	0.00	0.07	0.64	0.29	Few and very distorted KH structures; strong small-scale activity with λ_{KH}
0.750	0.00	0.01	0.64	0.34	Very few KH vortices; strong small-scale activity with λ_{KH}
0.8125	0.00	0.04	0.56	0.39	Very few KH vortices; very random
0.875	0.00	0.01	0.58	0.41	Quieter; very few KH vortices; very random
1.000	0.01	0.04	0.45	0.49	Quieter; very few KH vortices; very random

TABLE 3. Estimated frequencies of the four cases shown in figure 24; comparison of steady and unsteady flow behaviour.

Phase $t/t_0 = 0.375$. As the maximum free-stream velocity induced by the wake ('max U_{fs}') arrives at the front of the bubble, a significant number of the measurements are relatively quiet with very few fluctuations in the early portion of the boundary layer ($x/S_0 < 0.80$). Two examples of this quiet behaviour are plotted in figure 26 in the same manner as for figure 24. The maximum free-stream velocity induced by the wake is about to convect into the measurement window: it is, in fact, just upstream, at a streamwise location of $x/S_0 \approx 0.66$. The wall-normal vorticity (left-hand column) reveals only very weak Klebanoff streaks, while the wall-normal velocity and autocorrelation plots do not reveal any significant fluctuations. The quiet behaviour corresponds to the region of calmed flow observed in the hot-film data (figure 15*b*) and the instantaneous vorticity plots (e.g. figure 21) during this phase.

https://doi.org/10.1017/jfm.2011.204 Published online by Cambridge University Press

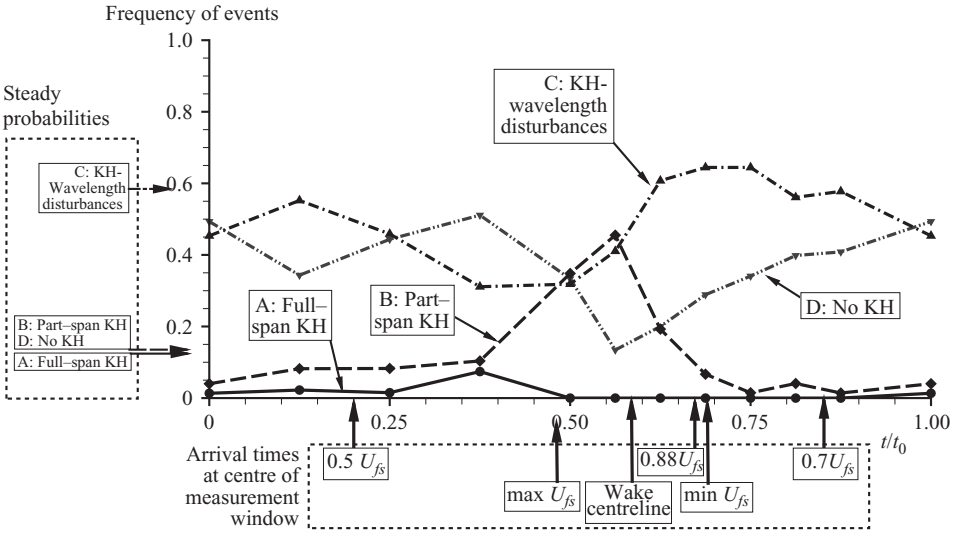


FIGURE 25. Estimated frequencies of the four cases shown in figure 24; comparison of steady and unsteady flow behaviour.

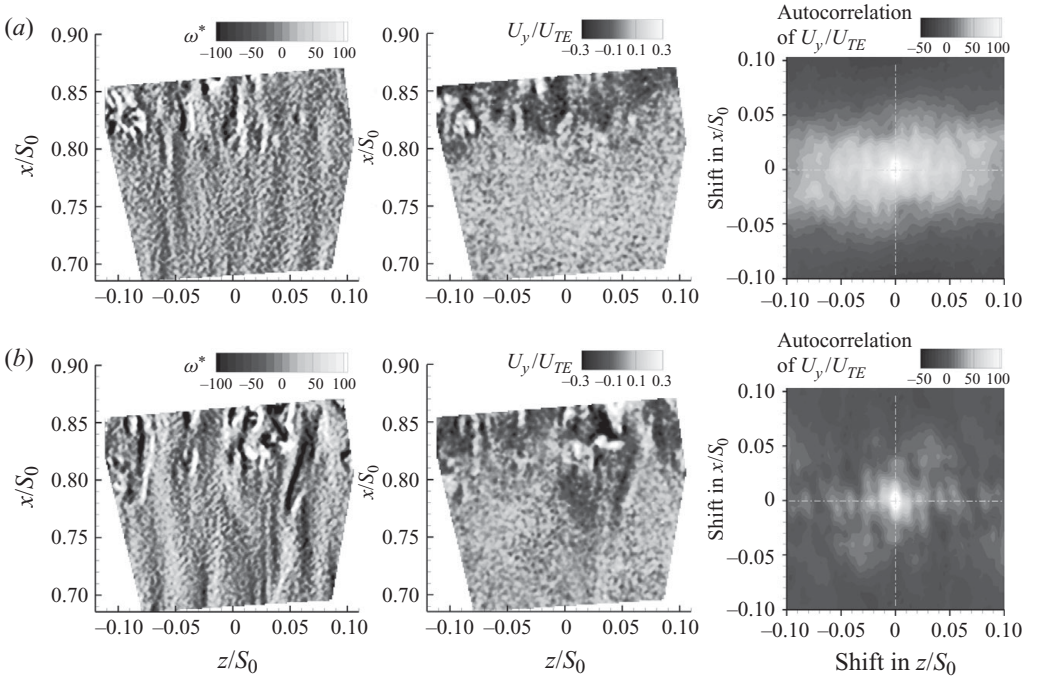


FIGURE 26. Two examples of instantaneous data $t/t_0 = 0.375$, $y/S_0 = 0.011$, showing the relatively quiet behaviour for $x/S_0 < 0.80$. The line of maximum velocity induced by the wake is just upstream of the window, at $x/S_0 \approx 0.66$.

Phase period $t/t_0 = 0.500$–0.5625. As the wake centreline passes over the bubble, a significant number of the measurements show part–span KH structures (table 3 and figure 25), many of which are similar in appearance to the three examples shown in figure 27 for $t/t_0 = 0.5625$. In the plots of wall-normal velocity, short-span

https://doi.org/10.1017/jfm.2011.204 Published online by Cambridge University Press

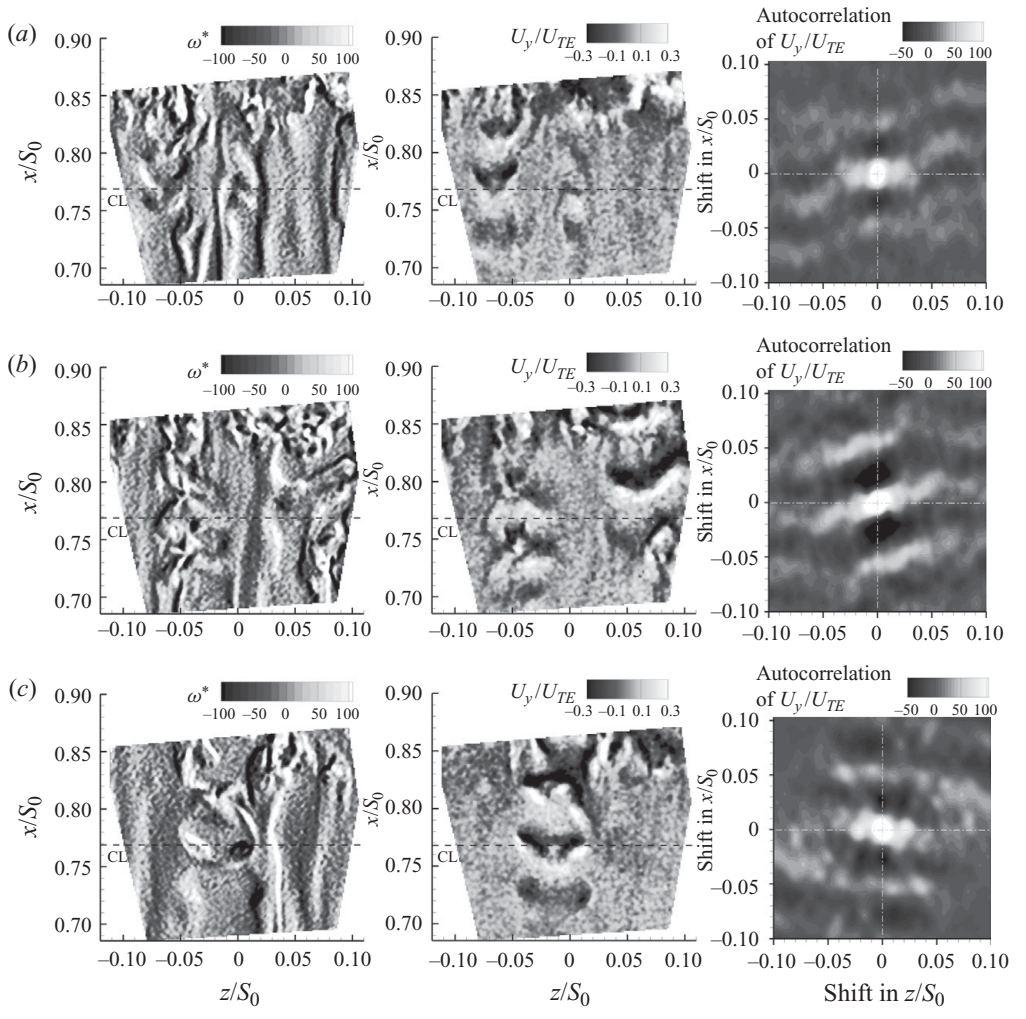


FIGURE 27. Three examples of instantaneous data as the wake centreline (CL) passes over the bubble, showing short-span KH structures, $t/t_0 = 0.5625$, $y/S_0 = 0.011$ (plane 2 in figure 11).

disturbances consisting of several peaks and troughs are observed; the autocorrelation plots confirm that these disturbances exhibit the KH wavelength. The nature of these structures and the likely inception mechanisms are discussed in detail in § 4.2.1 below.

Phase period $t/t_0 = 0.625$–0.750. As the region of minimum free-stream velocity induced by the wake passes over the separation bubble, there is a marked increase in the probability of case C (table 3 and figure 25), where small-scale fluctuations are observed at the KH wavelength. Three examples of the observed behaviour are shown in figure 28 for $t/t_0 = 0.750$. The autocorrelation plots clearly show the presence of the KH wavelength in the streamwise direction. As previously discussed for the steady flow results in figure 24, the tendency for disturbances to be spaced at the KH wavelength indicates the early stages of KH disturbance breakdown. The vorticity plots in figure 28 reveal the presence of wake-amplified Klebanoff streaks which are stronger than those observed in the previous time-step (figure 27).

The strong influence of the KH instability during this phase appears to result from the breakdown of the KH structures observed in previous time-steps (figure 27). The

https://doi.org/10.1017/jfm.2011.204 Published online by Cambridge University Press

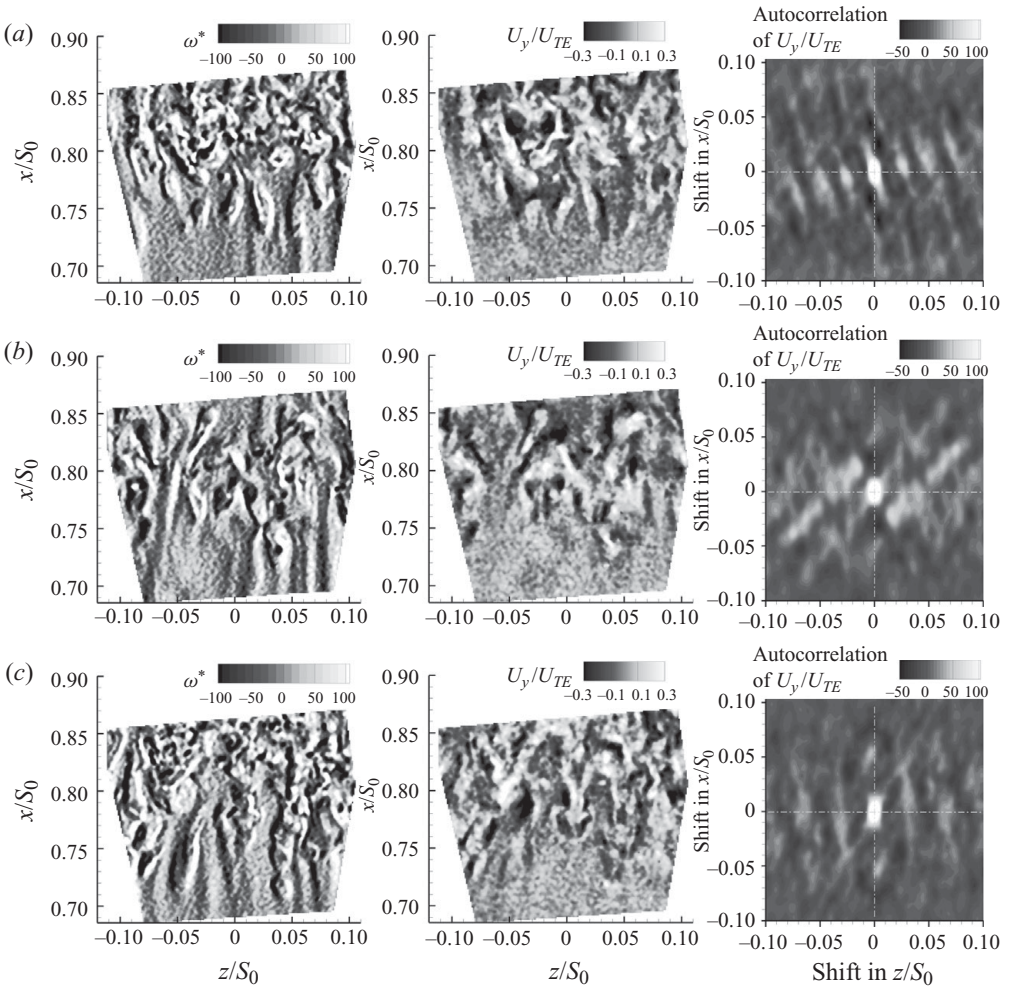


FIGURE 28. Three examples of instantaneous measurements showing disturbances at the KH wavelength, $t/t_0 = 0.750$, $y/S_0 = 0.011$ (plane 2 in figure 11*a*).

stability analysis in figure 23 suggested that the KH disturbances travel at around 50% of the free-stream velocity. The wake-amplified Klebanoff streaks propagate more quickly (at up to $0.88\,U_{fs}$), catching up with the KH structures and driving their breakdown to smaller scales. Indeed, the vorticity plots in figure 28 show the presence of strong Klebanoff streaks, and the autocorrelation plots show dominant spanwise wavelengths in the range 0.02–0.03 S_0, equating to the spacing between streaks. The role of the Klebanoff streaks and associated Λ-vortices in the breakdown of the KH structures has been indicated in the transition roadmap of figure 3 (process *e*).

Phase period $t/t_0 = 0.8125$–1.000. During these time-steps, the fluctuations in the flow become more random, indicated by the increased probability of case D (no clear KH disturbances) in table 3 and figure 25. These time-steps correspond to the arrival of the strongest wake-amplified Klebanoff streaks from the leading edge (along the $0.7\,U_{fs}$ path in figure 15), and the high frequency of case D indicates a more complete breakdown of the flow to small scales when compared to the previous time-steps.

https://doi.org/10.1017/jfm.2011.204 Published online by Cambridge University Press

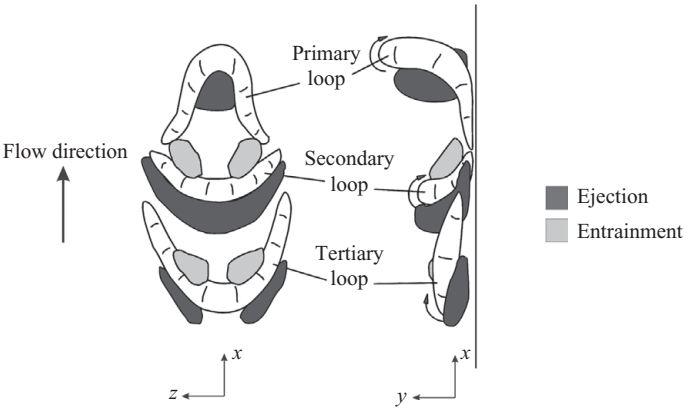


FIGURE 29. A schematic of a spot precursor in separated flow transition with elevated free-stream turbulence, after McAuliffe & Yaras (2010).

4.2.1. *Discussion: nature and inception of the part–span KH structures*

The flow structures in figure 27 are reminiscent of the developing KH wave packet studied by Watmuff (1999). Similar structures were also identified in the DNS simulations of separated flow transition at high free-stream turbulence levels by McAuliffe & Yaras (2010); a schematic of a typical structure is presented in figure 29, where the three vortex loops are spaced at the KH wavelength along the mid-span of the structure. The shapes of the flow structures in figure 27 are similar to those in figure 29. McAuliffe & Yaras (2010) argued that these structures originated in local instabilities in the distorted shear layer, which corresponded to the centrelines of Klebanoff streaks. The smoke visualisation performed by Asai *et al.* (2002) showed a similar flow pattern for the case of varicose (symmetric) streak instability, which exhibited a similar streamwise wavelength to the local KH wavelength instability of the boundary layer.

In the current measurements, numerous KH structures are observed directly underneath the centreline of the wake, during the period $t/t_0 \approx$ 0.5–0.6 (figure 25). These phases precede the arrival of the wake-amplified Klebanoff streaks, so only the weak Klebanoff modes induced by the free-stream turbulence are present in the separated shear layer when the KH structures are generated. During these phases, the free-stream velocity is strongly perturbed by the wake. For low free-stream turbulence levels, Wissink *et al.* (2006) demonstrated that this large-scale velocity perturbation generated full-span KH roll-up vortices in a separation bubble, suggesting that a similar process is underway in the current experiments. However, similar structures to those in figure 27 were very occasionally observed in the steady flow data (in around 1–2% of the measurements), two examples of which are presented in figure 30. It is therefore possible, though uncommon, for KH structures to form under the influence of free-stream turbulence alone, without the presence of the large-scale velocity perturbation of the wake.

It is therefore not clear from the current measurements exactly how the KH structures are generated, but two possible mechanisms can be proposed which fit the observations.

(i) Forcing by small-scale fluctuations: localised instabilities in the shear layer are induced by the weak Klebanoff streaks generated by the free-stream turbulence. The KH structures are generated when these instabilities are excited by small-scale velocity

https://doi.org/10.1017/jfm.2011.204 Published online by Cambridge University Press

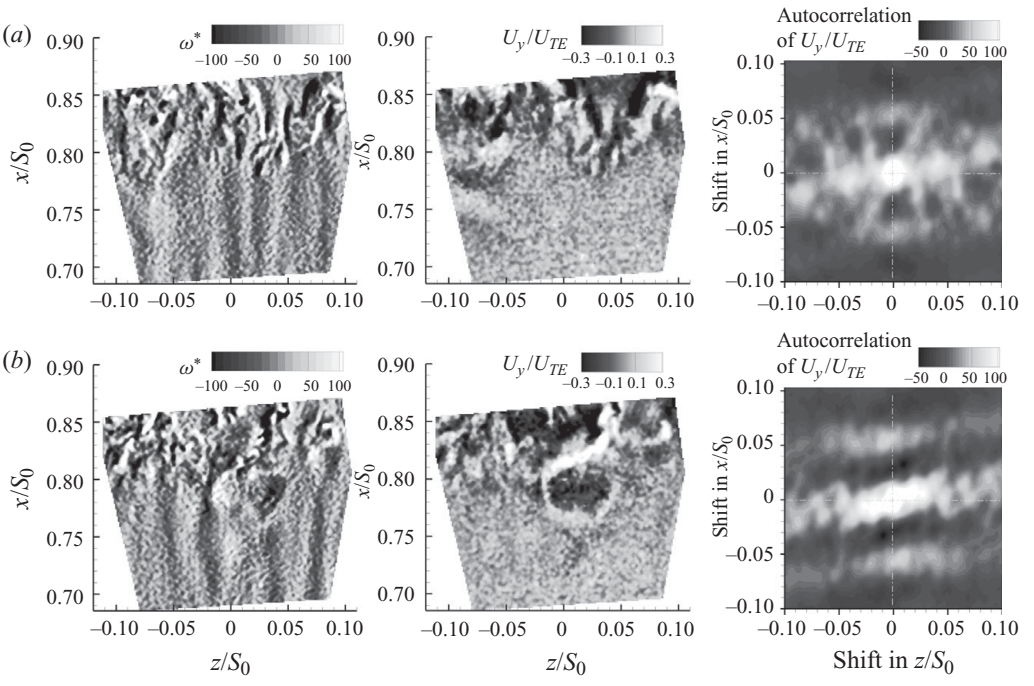


FIGURE 30. Two examples of weak and very occasional short-span KH structures in steady flow, $y/S_0 = 0.011$ (plane 2 in figure 11*a*).

fluctuations in the free stream. In steady flow, the elevated free-stream turbulence induces occasional KH structures, while the elevated turbulence in the wake induces a large number of structures under the wake path.

(ii) Modulation by the large-scale velocity perturbation: the KH structures emerge from the local inherent instabilities of the shear layer without the need for external forcing. The large-scale velocity perturbation induced by the wake encourages the production of KH structures, for example, by influencing the stability of the shear layer.

It is also possible that the KH structures are generated through a combination of these mechanisms. Further investigation of the inception process would likely require a numerical simulation. For example, the role of the large-scale velocity perturbation could be examined by performing a simulation with a laminar wake, similar to that performed by Wissink *et al.* (2006) but with elevated free-stream turbulence.

5. Summary and conclusions

The transition process in the suction surface boundary layer of low-pressure turbine blades is inherently unsteady and multi-modal. The wakes shed by the upstream blade row periodically convect over the boundary layer, causing both a large-scale perturbation in the free-stream velocity and an increase in the turbulence intensity at the boundary-layer edge. Between these passing wakes, the background turbulence level is also relatively high. Transition is driven by a complex interaction between the instabilities of the boundary layer and the free-stream disturbances.

The unsteady transition process has been modelled experimentally on a flat plate which features a laminar separation bubble, as is typical for modern high-lift blades.

https://doi.org/10.1017/jfm.2011.204 Published online by Cambridge University Press

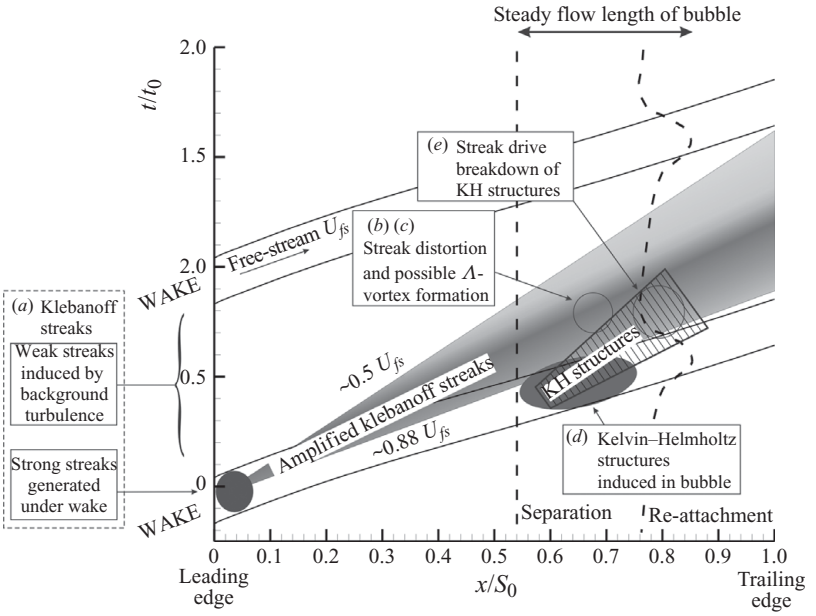


FIGURE 31. Space–time summary of the observed transition process.

The observed transition process has been summarised as a space–time diagram in figure 31, where the labels correspond to the relevant section of the transition diagram in figure 3. The free-stream turbulence (between wakes) induces relatively weak Klebanoff streaks in the boundary layer (process *a*), which are streamwise streaks with low velocity compared to the bulk of the flow. These structures originate in the thin boundary layer near the leading edge of the flat plate and are present throughout the unsteady flow cycle. The incoming wakes induce two different disturbances in the boundary layer which encourage early transition.

The elevated turbulence in the wake generates Klebanoff streaks which are significantly stronger than those generated by the background turbulence (process *a* in figure 31). A region of wake-amplified Klebanoff streaks originates close to the leading edge, convects downstream at a fraction of the free-stream velocity and spreads in the streamwise direction. The celerity rates are very similar to those observed for turbulent spots, with leading and trailing edge celerity rates of around 88% and 50% of the free-stream velocity. The strongest wake-amplified Klebanoff streaks travel at around 70% of the free-stream velocity. The Klebanoff streaks can induce transition to turbulent flow via the production and breakdown of Λ-vortices (processes *b* and *c* in figures 31 and 3). The region of wake-amplified Klebanoff streaks is associated with a region of elevated momentum thickness, which in a real turbine will reduce the efficiency. Since the wake-amplified Klebanoff streaks travel more slowly than the wakes, these effects lag significantly behind the wake as it convects over the boundary layer.

As the wake passes over the laminar separation bubble, it induces a second type of disturbance by exciting the KH instability of the separated shear layer, inducing the formation of short-span KH structures (process *d* in figures 31 and 3). This process is distinct from the full-span roll-up of the shear layer which has been previously observed at low free-stream turbulence levels. The KH structures are similar in

https://doi.org/10.1017/jfm.2011.204 Published online by Cambridge University Press

appearance to flow structures previously identified in direct simulations of separated flow transition with elevated free-stream turbulence by McAuliffe & Yaras (2010).

It is evident that the wake-amplified Klebanoff streaks do not play a role in the inception of the KH structures, since they do not arrive in the separated shear layer until later in the wake cycle. Rather, it is the weak Klebanoff streaks generated by the free-stream turbulence that are present in the shear layer when the KH structures form. It is not clear from the data whether it is the small-scale turbulence or the large-scale velocity fluctuation of the wake that causes the KH structures to be generated. A further numerical study is proposed to investigate the inception mechanism in more detail.

The breakdown of the KH structures to small-scale turbulence is driven by the arrival of the wake-amplified Klebanoff streaks from the leading edge (process *e* in figure 31), which convect more quickly. The bubble remains shorter than its steady length until the wake-amplified streaks have convected past; it is therefore the streaks that are largely responsible for the time-mean reduction in the size of the bubble. After the wake-amplified streaks have convected past the separation bubble, transition starts to move further aft on the surface under the influence of a calmed flow region, similar to that observed behind 'classical' Emmons-style turbulent spots. Relatively quiet flow behaviour is observed in the instantaneous data during this time. At the wake frequency investigated, the arrival of the subsequent wake interrupts the calmed flow region.

The authors would like to thank the technical staff at the Whittle Laboratory for their help with the experimental set-up and G. Walker of the University of Tasmania for his valuable input. The Rayleigh stability code was kindly provided by O. N. Ramesh and S. S. Diwan of the Indian Institute of Science, whose help is gratefully acknowledged. Thanks are also due to EPSRC and Rolls-Royce for funding this investigation.

REFERENCES

Alfredsson, P. H. & Matsubara, M. 1996 Streaky structures in transition. In *Transitional Boundary Layers in Aeronautics* (ed. R. Henkes & J. van Ingen), pp. 374–386, Elsevier.

Asai, M., Minagawa, M. & Nishioka, M. 2002 The instability and breakdown of a near-wall low-speed streak. *J. Fluid Mech.* **445**, 289–314.

Cai, C. & Harrington, P. B. 1998 Different discrete wavelet transforms applied to denoising analytical data. *J. Chem. Inf. Comput. Sci.* **38** (6), 1161–1170.

Coull, J. D. & Hodson, H. P. 2010 Predicting the profile loss of high lift low pressure turbines. *ASME Paper GT2010-22675*.

Coull, J. D., Thomas, R. L. & Hodson, H. P. 2010 Velocity distributions for low pressure turbines. *Trans. ASME, J. Turbomach.* **132** (4), 041006.

Diwan, S. S. & Ramesh, O. N. 2009 On the inflectional instability of a laminar separation bubble. *J. Fluid Mech.* **629**, 263–298.

Durbin, P. A., Zaki, T. A. & Liu, T. 2009 Interaction of discrete and continuous boundary layer modes to cause transition. *Intl J. Heat Fluid Flow* **30**, 403–410.

Ginoux, J. 1965 Streamwise vortices in laminar flow. In *Proc. AGARDoGRAPH '97*, Part II, Paris.

Halstead, D. E. 1996 Boundary layer development in multi-stage low pressure turbines PhD thesis, Iowa State University.

Hodson, H. P. 1983 The detection of boundary layer transition and separation in high speed turbine cascades In *Proc. Seventh Symp. Measurement Techniques for Transonic and Supersonic Flow*, Aachen, Germany, 21–23 September.

Hughes, J. D. & Walker, G. W. 2001 Natural transition phenomena on an axial compressor blade. *J. Turbomach.* **123** (2), 392–401.

https://doi.org/10.1017/jfm.2011.204 Published online by Cambridge University Press

Inger, G. R. 1975 Three dimensional disturbances in reattaching separated flows. In *Proc. AGARD Conf.*, no. 168, Gottingen.

Jacobs, R. G. & Durbin, P. A. 1998 Shear sheltering and the continuous spectrum of the Orr–Sommerfeld equation. *Phys. Fluids* **10** (8), 10.1063/1.869716.

Jacobs, R. G. & Durbin, P. A. 2001 Simulations of bypass Transition. *J. Fluid Mech.* **428**, 185–212.

Lewalle, J., Ashpis, D. E. & Sohn, K.-H. 1997 Demonstration of wavelet techniques in the spectral analysis of bypass transition data. NASA Technical Publication 3555.

Marxen, O., Lang, M., Rist, U., Levin, O. & Henningson, D. S. 2009 Mechanisms for spatial steady three-dimensional disturbance growth in a non-parallel and separating boundary layer. *J. Fluid Mech.* 634, 165–189.

Matsubara M., & Alfredsson, P. H. 2001 Disturbance growth in boundary layers subjected to free-stream turbulence. *J. Fluid Mech.* **430**, 149–168.

McAuliffe, B. R. & Yaras, M. I. 2010 Transition mechanisms in separation bubbles under low and high freestream turbulence. *Trans. ASME, J. Turbomach.* **132** (1), 011004.

Opoka, M. M. & Hodson, H. P. 2008 Experimental investigation of unsteady transition processes on high-lift T106A turbine blades. *J. Propulsion Power* **24** (3), 424–432.

Orth, U. 1993 Unsteady boundary-layer transition in flow periodically disturbed by wakes. *Trans. ASME, J. Turbomach.* **115** (4), 707–713.

Pfeil, H., Herbst, R. & Schröder, T. 1982 Investigations of the laminar-turbulent transition of boundary layers disturbed by wakes *ASME Paper 82-GT-0406.*

Roshko, A. & Thomke, G. J. 1966 Observations of turbulent reattachment behind an axi-symmetric downstream facing step in supersonic flow. *AIAA J.* **4**, 975–980.

Schlichting, H. 1979 *Boundary Layer Theory*. 7th edn. McGraw-Hill

Schubauer, G. B. & Klebanoff, P. S. 1955 Contributions on the mechanics of boundary layer transition. NACA TN 3489 and NACA rep1289.

Solomon, W. J., Walker, G. J. & Hughes, J. D. 1999 Periodic transition on an axial compressor stator: incidence and clocking effects: Part II – Transition onset predictions. *Trans. ASME, J.Turbomach.* **121** (3), 408–415

Stanislas, M., Okamoto, K., Kähler, C. J. & Westerweel, J. 2005 Main results of the Second International PIV Challenge. *Exp. Fluids* **39**, 170–191. (see also p. 35 and p. 37 of the Minutes of the Second International PIV Challenge: http://www.univ-lille1.fr/pivnet/sig32/min_chal_2003/minutes_challenge03_3.pdf)

Stieger, R. D. & Hodson, H. P. 2004 The transition mechanism of highly loaded low-pressure turbine blades. *Trans. ASME, J. Turbomach.* **126** (4), 536–543.

Stieger, R. D. & Hodson, H. P. 2005 The unsteady development of a turbulent bar wake through a downstream low-pressure turbine cascade. *Trans. ASME, J. Turbomach.* **127** (2), 288–394.

Watmuff, J. H. 1999 Evolution of a wave packet into vortex loops in a laminar separation bubble. *J. Fluid Mech.* **397**, 119–169.

Wheeler, A. P. S., Sofia, A. & Miller, R. J. 2007 The effect of leading-edge geometry on wake interactions in compressors. *ASME Paper GT2007-27802.*

White, F. M. 1999 *Viscous Fluid Flow* 2nd edn. McGraw-Hill.

Wissink, J. G., Rodi, W. & Hodson, H. P. 2006 The influence of disturbances carried by periodically incoming wakes on the separating flow around a turbine blade. *Intl J. Heat Fluid Flow* **27**(4).

Wu, X., Jacobs, R. G., Hunt, J. C. R. & Durbin, P. A. 1999 Simulation of boundary layer transition induced by periodically passing wakes. *J. Fluid Mech.* 398, 109–153.

Yarusevych, S., Kawall, J. G. & Sullivan, P. E. 2008 Separated-shear-layer development on an airfoil at low reynolds numbers *AIAA J.* **46** (12), 3060–3069.

Zhang, X. F. & Hodson, H. P. 2007 Effects of Reynolds number and freestream turbulence intensity on the unsteady boundary layer development on an ultra-high-lift airfoil. *ASME Paper GT2007-27274.*

Zhang, X. F., Hodson, H. P. & Harvey, N. W. 2005 Unsteady boundary layer studies on ultra-high-lift low pressure turbines *Proc. IMechE, Part A: J. Power and Energy* **219**, 451–460.

https://doi.org/10.1017/jfm.2011.204 Published online by Cambridge University Press